UiT
THE ARCTIC
UNIVERSITY
OF NORWAY

Faculty of Science and Technology
Department of Physics and Technology

Ice-water Classification in the Barents Sea from Sentinel-1 EW SLC Images

August Krokan

EOM-3901 Master thesis in Energy, Climate and Environment 30 SP

June 2019

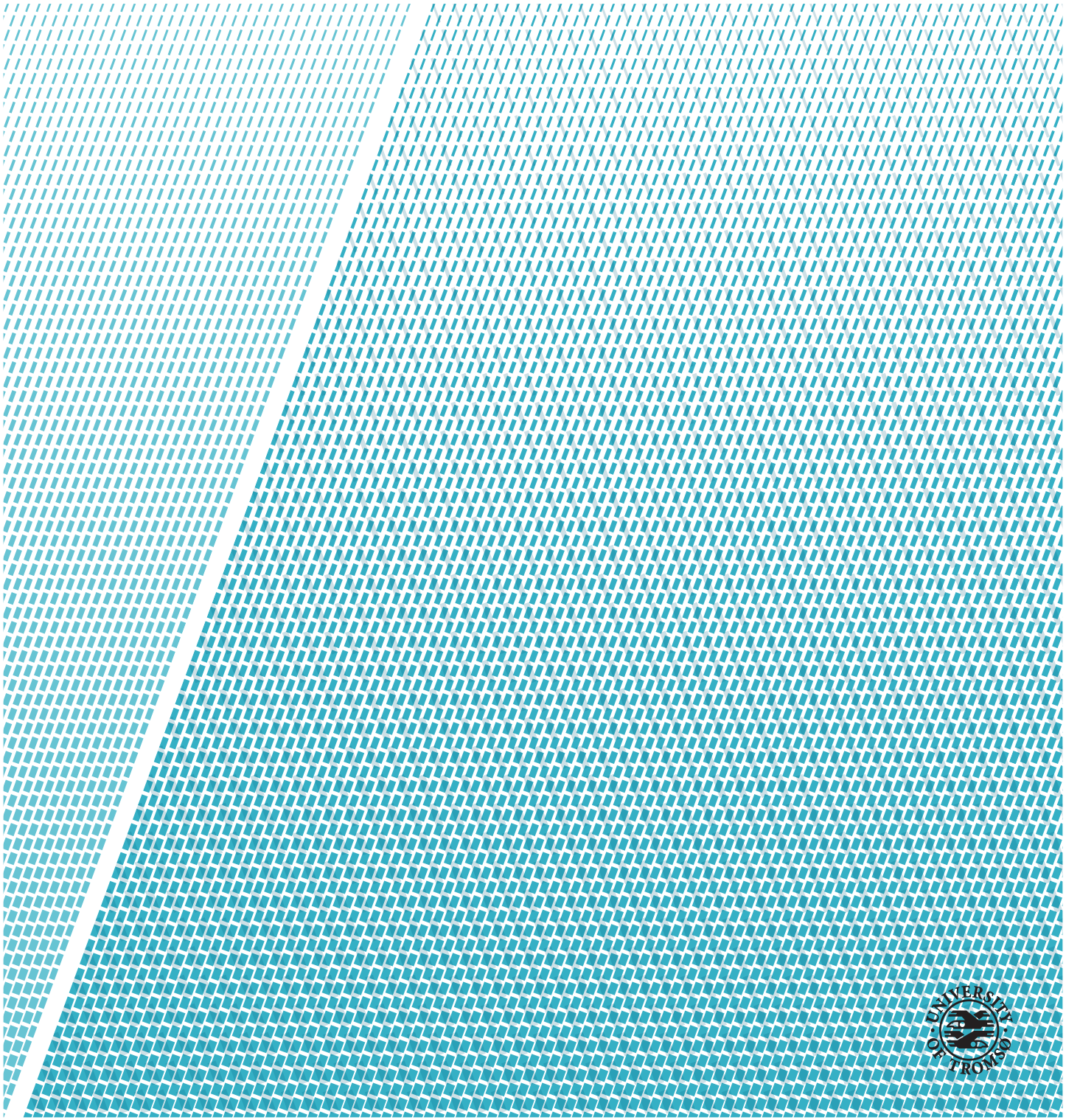

Abstract

The focus of this thesis is to do ice-water classification on Sentinel-1 EW SLC imagery using an unsupervised Mixture of Gaussian segmentation algorithm. The classes are automatically labelled as sea ice or water based on the slope of the observed brightness decay from near- to far-range, which is different for sea ice and water. The aim of the thesis is twofold. In the first part, the ability of seven features to separate between ice and water are evaluated. It turned out that a combination of geometric brightness, cross-polarization ratio and relative kurtosis gave highest accuracy - 99.29 %. In the second part, the goal was to find the highest achievable, reliable resolution on the classified ice-water maps. The purpose is to find out how little it is possible to multi-look and still achieve high enough radiometric resolution to discriminate ice and water in a satisfactory manner. It turned out that a resolution of 46x43 meter with moderate accuracy is obtainable if swath 1 is omitted. This require SLC imagery. Alternatively, 93x87m resolution with better ice-water separation and higher accuracy can be obtained. The classified image can be used to derive other ice information products, such as ice concentration. This was demonstrated both with low and high resolution, and compared with hand drawn ice concentration maps from the Meteorological Institute.

Acknowledgements

First of all, I would like to thank my supervisor, Professor Torbjørn Eltoft for your guidance and ideas throughout my time working on this thesis.

I am also very grateful to Associate professor Anthony Doulgeris for all discussions, helpful feedback and for supplying me with codes I needed for this project. Your assistance during the last period of the project was invaluable.

Furthermore, I also wish to thank Thomas, Johannes and Vebjørn at CIRFA for all your help whenever I ran into troubles, which was pretty often.

And last but not least I would like to thank my friends, family and Karlotte for your love and support, especially during the last months.

Contents

List of Figures

List of Tables

1 Introduction

1.1 Motivation

Arctic sea ice has a global influence on the Earth's climate, mainly by insulating the relative warm ocean from the cold polar atmosphere and increasing the surface albedo (Marshall and Plumb, 1989). Changes in sea ice extent can be an important indicator of climate change, and the last decades we have seen a transformation towards thinner and younger sea ice (Masson-Delmotte et al., 2018) (Johannessen et al., 2006). This development enables ships and maritime installations into new waters, which is of great interest for several different industries, including oil, fishing and tourism. Increased traffic in Arctic waters in the future is therefore expected. However, safe transportation in or near ice-infested waters require knowledge about the location and condition of the sea ice (Meier and Stroeve, 2008). Ice conditions in the Arctic are continuously changing due to ice drift, up to 50 km per day (Johannessen et al., 2006), and the temporal validity of ice maps is therefore generally short (Onstott and Shuchman, 2004). Hence, reliable and frequent mapping of sea ice is needed.

However, in situ data collection for ice maps is a demanding task in the Arctic due to the hostile climate, the remoteness and - of cource - its immense size. The use of optical sensors is also limited, as Arctic is under darkness for a longer period of the year and clouds obscure the area near the ice edge about 70% of the time (Onstott and Shuchman, 2004). Synthetic Aperture Radar (SAR) is an active microwave remote sensing system that overcome these problems, as it

provides its own illumination, enabling it to provide large-scale, high-resolution imagery under almost any weather and environmental conditions at any time. SAR imagery is therefore an important source for studying climate change, as well as biological-ecological and physical processes, and supporting navigation of ships or other activities in ice-infested waters.

Sea ice can be separated from water in SAR images based on the variation in the intensity of the backscattered radar signal. Generally, sea ice gives a stronger return signal than water and will thus look brighter in the SAR image. There is, however, some exceptions. Backscatter intensity from ice and water can take a broad range of values, depending on many factors, including geophysical properties of the ice/water, wind, temperature and precipitation. Thus, ice-water separation is sometimes impeded by ambiguities, as different sea ice types and open water can have similar backscatter signatures. In particular, discrimination of rough water and multi-year ice, or calm water and smooth first year ice, is often problematic as they have similar backscatter intensity (Zakhvatkina et al., 2017). Accordingly, designing an automated ice-water classification scheme is not a straight forward task, as a robust automated ice-water classifier must be able to cover the broad variety of backscatter intensities of sea ice and water under variable and changing surface conditions. For that reason, sea ice concentration maps are currently primarily produced manually by ice expert analysts (Zakhvatkina et al., 2019). The Norwegian Ice Service produce ice concentration maps five days a week, which is a cumbersome and time-consuming task. Efforts are being made to make reliable automatic ice maps, but to the author's knowledge there is no reliable automatic ice concentration maps that is operational at present (Wang et al., 2016). There is therefore a need to improve automatic ice-water classification.

A way to improve ice-water classification can be to add extra image characteristics, or features, to the classification process (Zakhvatkina et al., 2017). Texture features are widely used as extra features, as they consider not only the brightness, but also the spatial variation in the image. Also, different combinations of the polarimetric channels, i.e. polarimetric features, can be used. (Doulgeris, 2013) presented a method of extracting 6 polarimetric features by the extended polarimetric feature space (EPFS) method. These features require quad-pol data. Such data is not applicable for operational use, due to its narrow swath width. Three of the features can, however, be extracted for dual-pol, which is more useful for operational use to due its higher coverage (Scheuchl et al., 2004). These features; geometric brightness, cross-polarization ratio and relative kurtosis, have been proven to work well for separation between different ice types (Fors et al., 2016), (Doulgeris, 2013). Their effectiveness to separate solely between ice and water has not, to the author's knowledge, been investigated to the same degree. The first part of the thesis is to evaluate the effectiveness of these features in ice-water classification. Moreover, two other features from the

covariance matrix, that not is found too much information about in literature when it comes to ice-water classification, are evaluated. These features are the magnitude and angle of the HH-HV correlation (off-diagonals in the covariance matrix), and their utility for ice-water separation will be investigated.

The second part of this project will be an investigation of spatial resolution of ice-water classification. The spatial resolution of ice information products can in some cases be crucial for ship routing. Requirements for sea ice information for operational use are often defined into two types; tactical and strategical (Scheuchl et al., 2004). Strategical ice information is used to assist ships in preliminary route planning, and resolution is rather course (1 km). Tactical ice information on the other hand, refers to the level of detail required to support ship navigation in ice (Scheuchl et al., 2004). The main goal of tactical ice information is to choose the optimal course through the ice, both by finding leads and cracks in the ice, and by avoiding dangerous ice phenomena such as intensive ice drift and ice bergs (Johannessen et al., 2006). The user requirements for such maps is strict when it comes to spatial and temporal resolution, in order to capture small scale sea ice features. Tactical ice navigation should therefore, according to (Johannessen et al., 2006), be based on satellite data with a spatial resolution of 50-100 meters or better.

Sentinel-1 data, which is used in this project, is provided either as single-look complex (SLC) or ground-range, multi-looked, detected (GRD) images. SLC is superior to GRD when it comes to spatial resolution (93x87m vs 8-15x43m), but suffers from speckle noise. The question is if SLC images, despite its noise, can be used for ship navigation, where the requirement of spatial resolution is high, or if the speckle makes the classified ice-water images useless. In that case, how much do the classified image have to be multi-looked in order to be usable for ship navigation. In other words, what is the best achievable resolution on ice-water classification using SLC images, where the image interpretation and classification is not disturbed too much by speckle.

1.2 Objective and contribution to the field

In this project, the objective is to do ice-water classification on Sentinel-1 Extra-wide SLC images in the Barents Sea, using an unsupervised mixture of Gaussian segmentation algorithm and label the classes based on the slope of the brightness decay from near- to far range of each class. The aim of the work is twofold. The first is to evaluate the effectiveness of a set of features derived from the covariance matrix. These features are geometric brightness, cross-polarization ratio and relative kurtosis. In addition, correlation coefficients between the two channels, in particular HH-HV correlation magnitude and

angle, will be evaluated. The results of the ice-water classifications, using different combinations of these features, will be evaluated by visual inspection and compared with a ground truth to obtain an accuracy score. The second aim is to investigate what is the highest achievable, reliable ice-water classification resolution, that can be obtained using Sentinel-1 EW SLC images.

Specific tasks include

- Evaluating the utility of geometric brightness, cross-polarization ratio, relative kurtosis, HH-HV correlation magnitude and HH-HV correlation angle for ice-water classification.
- Determining what is the highest achievable resolution on ice-water classification, where the classified image not is corrupted too much by noise.
- Purpose a method for removing additive thermal noise from EW SLC images in order to increase classification accuracy on ice-water maps.
- Make an ice-concentration map based on the classified ice-water image and compare it to the manually drawn ice maps made by the meteorological institute.

These tasks will together, hopefully, contribute to the field both by providing an approach to produce as accurate automatic ice-water classification as possible and by explaining what is the highest spatial resolution achievable on ice-water maps using Sentinel-1 EW SLC images.

1.3 Structure of thesis

Chapter 2 gives an introduction to SAR theory. This includes a brief introduction to the basic SAR principles, the image geometry, the radar equation, resolution, frequency, speckle, polarization, scattering and the TOPSAR technique.

Chapter 3 describes the physics behind SAR measurements of sea ice and water.

Chapter 4 describes the data and the area of interest.

Chapter 5 illustrates the method used in this thesis.

Chapter 6 is a presentation of the results and a discussion

Chapter 7 is a conclusion.

2

SAR theory

2.1 SAR principles

Remote sensing is defined as the method of acquiring information about an object or phenomena without coming into physical contact with it. For the purpose of Earth observation, this is done by using air- or spaceborne sensors to detect and measure electromagnetic radiation in the range from ultraviolet to microwave, coming from the Earth. By studying properties of the radiation such as intensity, frequency, phase and polarization, one can obtain valuable information about the physical properties of the surface which can be used to separate and classify different Earth features.

The sensors used for Earth observation can be divided into two main types based on its use of electromagnetic spectral regions; namely optical (UV to infrared) and microwave, each having its limitations and capabilities for remote sensing (Elachi and Van Zyl, 2006). The sensors can again be divided into passive and active sensors. Passive satellites measure the natural radiance coming from the Earth, whilst active satellites provide its own illumination and can therefore be used regardless of sun illumination. Synthetic aperture radar (SAR) is a type of system that belong to the class of active microwave imaging systems. SAR works by employing an antenna to transmit a radar signal at a given frequency towards a portion of the Earth's surface and then record the signal reflected back to the sensor. The backscattered energy is then used to form an image of the illuminated surface. The stronger the backscatter signal

from a certain area is, the brighter this area will appear in the image.

Most microwave sensors operate in the range from 1mm to 1m wavelengths. These wavelengths are much longer than the size of particles and gases in the atmosphere, and microwaves will therefore penetrate through cloud cover, dust, haze and most weather conditions except for heavy rainfall. This property is very important for remote sensing as it allows microwave sensors to be used under almost any weather and environmental conditions, day or night (Campbell and Wynne, 2011). SAR is therefore the premier sensor for a number of different Earth observation applications.

2.2 Imaging geometry

As illustrated in fig 2.1, SAR is a side-looking system, i.e. it acquires images by transmitting energy pulses perpendicular to the direction of the flight path of the moving platform. This configuration is necessary in order to eliminate right-left ambiguities that would occur for two symmetric equidistant points for a nadir-looking system (Elachi and Van Zyl, 2006). Since the speed of microwaves is known, a SAR system can precisely measure the distance to an object by timing the delay between the transmitted and received signal (Campbell and Wynne, 2011). The sensor illuminates narrow strips of the surface, and these image strips are, as the satellite passes by, merged together to form a two-dimensional image.

One dimension corresponds to the time difference between the transmitted and received signal, in the direction called slant range. For convenience, however, the signals can be converted to ground range format, where distances are presented in their correct relative position on ground. The second dimension is referred to as azimuth direction, equal to the along track. In this direction, the signals can be separated using the Doppler history. This is possible because the large beam width of the radar will illuminate and linearly traverse an object on the surface for a lengthened period of time. The relative frequency of the signal will then be high when the satellite moves towards a target and decrease as the satellite moves away. During this period, the SAR collects information about phase and Doppler shift that, through signal processing, allows for a synthetic aperture to be created. If the source location of the signal in the azimuth direction is known, the resolution in azimuth is as accurate as observing the scene with an antenna the same size as the initial and final phases of the satellite track (Elachi and Van Zyl, 2006). Thus, fine spatial azimuth resolution can be achieved, even from space.

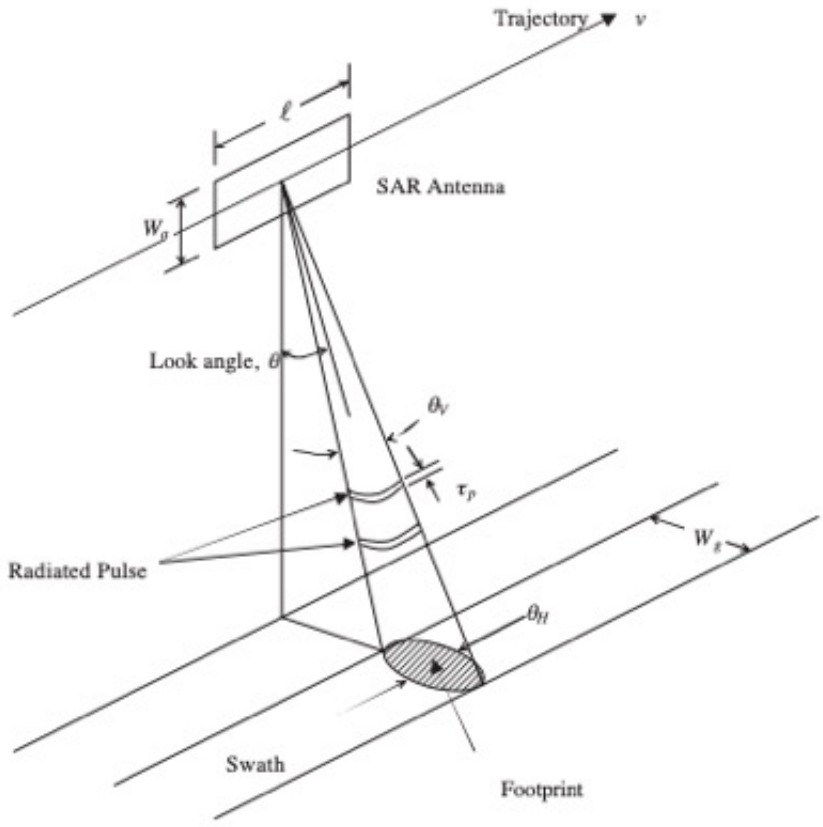

Figure 2.1: Imaging geometry. Figure from (Chan and Koo, 2008)

2.3 Radar equation

As mentioned, a radar works by transmitting microwave energy pulses into a small range of angles and then records the backscattered signal coming from different objects within the system's field of view. The interaction of the energy pulse with its targets, i.e. the relationship between the transmitted power Pt and the incoming power Pg is, together with the characteristics of the radar, described by the radar equation. To define this equation, we must first define the total power incident on an object at ground level, given as

$$P_g = \frac{P_t A_g G_t}{4\pi R^2} \quad (1)$$

where P_g is the power incident on the target, P_t is the transmitted power, A_g is the effective area of the target and G_t is the antenna gain given as

$$G_t = \frac{4\pi A_t}{\lambda^2} \quad (2)$$

The factor $\frac{1}{4\pi R}$ represents the reduction in power density as slant range increases.

Vice versa, the total power received by the sensor is given by

$$P_r = \frac{P_{g'} A_t G_g}{4\pi R^2} \quad (3)$$

where P_r represents the total received power at the sensor, A_t is the effective area of the receiver, and G_g represents the ground gain in the sensors direction. Again, 4π represents the reduction in power density, now assuming that the ground scatters power equally in all directions.

The equations (1) and (3) can be combined to determine a link between P_r and P_t, which is known as the radar equation (for a monostatic system):

$$P_r = \frac{G_r^2 \sigma \lambda^2}{(4\pi)^3 R^4} P_t \quad (4)$$

Where λ is the operating wavelength and σ is the radar cross section (RCS), that is, the ratio of the energy received by the sensor over the energy that would have been received if the target had scattered in an isotropic fashion (equally in all directions). The RCS is usually given is decibels, meaning that positive numbers imply that the surface is focusing energy towards the sensor, while negative numbers imply the opposite, that most of the energy is focused

away from the sensor (Elachi and Van Zyl, 2006). This quantity incorporates the slope, area, roughness and dielectric properties of the target into a single factor, and is given as

$$\sigma = 4\pi r^2 \frac{\left|\overrightarrow{E_s}\right|^2}{\left|\overrightarrow{E_l}\right|^2} \quad (5)$$

where E_s and E_l is the power of the scattered and incident electromagnetic waves, respectively, and r describes the distance between the sensor and the target.

From the radar equation, it is clear that one can increase the received power by increasing the antenna size A, or using shorter wavelengths λ. This is however balanced by the fact that the atmosphere limits the available wavelengths and large antennas are impractical to carry on aircrafts or satellites (Philpot and Philipson, 2012).

2.4 Resolution

The resolution of a radar system can be defined as its ability to distinguish between two objects separated by some minimum distance. If the two objects are sufficiently separated, they are displayed in two different resolution cells (pixels). Otherwise, the pixel will be a complex combination of the scattered energy from the two objects (Onstott and Shuchman, 2004). When considering SAR systems, it is important to distinguish between spatial resolution in range and azimuth direction, due to the fundamental differences in the way the images are acquired.

2.4.1 Resolution in range

Spatial resolution in range direction is a function of the effective pulse width τ. This is because two objects on the ground can only be distinguished if the echoes are received at different times. Since the pulse travels two ways, the two objects can be separated if the distance is larger than $\frac{\tau}{2}$. Thus, the range resolution is given as

$$Range\ resolution = c\frac{\tau}{2} \quad (6)$$

Where c is the speed of light, i.e. also the speed of the transmitted signal. From the equation it is clear that radar pulse width should be as short as possible to

achieve the finest resolution. However, shorter pulse width implies lower energy. In order to maintain an energy level high enough to distinguish the signal from the noise, the amplitude must be increased. The equipment required to transmit short, high-energy pulse is however hard to assemble. As a remedy, one can instead use a "chirp" approach, where the short pulse with constant frequency is replaced with a long pulse with modulated frequency. This method is utilized by SAR. The signal can then be processed after reception to focus the pulse to a much shorter value, which gives the same result as using a short pulse throughout the system (Elachi and Van Zyl, 2006).

2.4.2 Resolution in azimuth

Before SAR, Real Aperture Radars (RAR) were used for air-borne remote sensing. The azimuth resolution for RAR is given as

$$X_a = \frac{h\lambda}{Acos(\theta)} \quad (7)$$

Where h is the height above ground, λ is the wavelength, A is the antenna length and θ the incidence angle. Such radars are, however, impractical for remote sensing, since higher resolution only can be achieved by
1) Using shorter wavelengths, which is limited by clouds and atmosphere attenuation, or
2) Increasing the antenna length, which is practically impossible as it requires unrealistically long antennas, typically hundreds of meters long, in order to achieve descent resolution from space.
SAR overcomes this problem by using the forward motion of the radar to synthesize a longer antenna. It can be shown that an array of antennas lying in a single line is equivalent to a single antenna moving along that line (Elachi and Van Zyl, 2006). If we assume that the radar sensor is moving at a velocity v with an antenna of length L, the antenna main beam footprint on the surface will then be equal to

$$L' = 2\frac{\lambda h}{A} \quad (8)$$

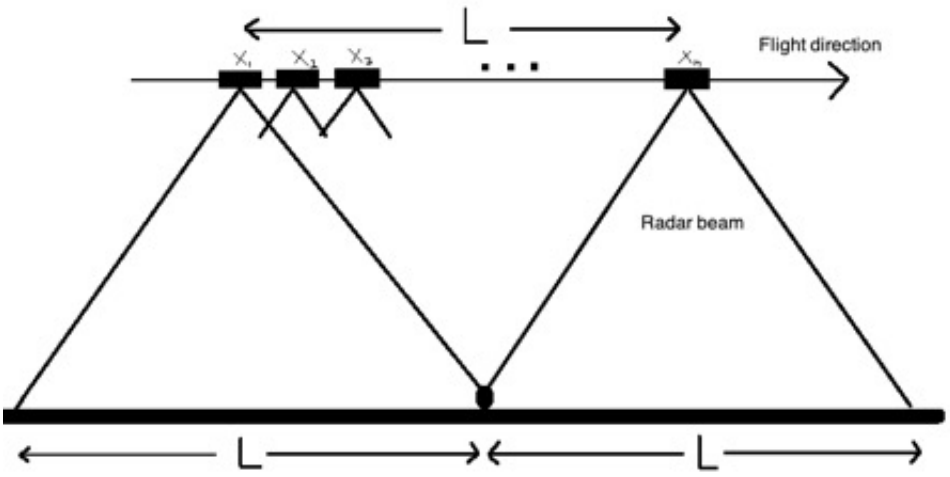

Figure 2.2: Azimuth resolution

As the radar passes a given target, consecutive pulses are scattered in sequence along the line of movement. These echoes are then processed together to synthesize a linear array. From fig 2.2 it is clear that the maximum array length that can be achieved is equal to L. The synthesized array will then have a beam width given as

$$\theta_s = \frac{\lambda}{L} = \frac{A}{2h} \quad (9)$$

which results in a footprint on the ground given as

$$X_a = h\theta_s = \frac{L}{2} \quad (10)$$

corresponding to the azimuth resolution. The equation may seem counterintuitive, as it suggests that the finest resolution is achieved by using a smaller antenna. In addition, the resolution is independent of the height of the sensor. The reason for this is that the farther away the sensor is, the larger will the footprint on the ground be, and consequently a longer synthetic array and finer resolution is achieved. The independence of height is caused by the fact that the finer synthetic beam will counterbalance the increase in height exactly.

2.5 Frequency

SAR instruments operates in the microwave region with wavelengths from approximately 1 mm to 1 m. The microwave region is further divided into smaller bands as shown in table 2.1. The use of the bands K and K_a for Earth

Radar Band Designation	Frequency Range (GHz)	Wavelength Range (cm)
P	0.230-1	130-30
L	1-2	30-15
S	2-4	15-7.5
C	4-8	7.5-3.75
X	8-12.5	3.75-2.40
Ku	12.5-18	2.40-1.67
K	18-26.5	1.67-1.13
Ka	26.5-40	1.13-0.75

Table 2.1: Radar frequencies

observation is however limited, due to the influence of clouds and atmosphere on such wavelengths. At 22 GHz, for instance, there is a water vapour absorption band that reduces transmission to 85 % (Chan and Koo, 2008). The most used bands for Earth observation from satellites are therefore P to K_u bands, and primarily L, C, X and K_u (Dierking, 2013), all having an atmospheric transmission close to 100 % (see figure 2.3).

The choice of band for SAR instruments is based on the purpose of the mission. The interaction mechanism between the radar wave and the target depends, among other factors, on the chosen frequency. This is due to the fact that waves interact strongly with targets with geometry of the same size as the radar wavelength. Also, the penetration depth of the incident wave is directly proportional to the wavelength (Elachi and Van Zyl, 2006). Accordingly, shorter wavelengths such as X band ($\lambda \sim$ 3 cm) will interact with smaller targets on the ground and will have low penetration capability. The opposite is true for longer wavelengths such as L band ($\lambda \sim 23$ cm), which will interact with bigger targets and have higher penetration depth. For sea ice monitoring, C-band offers a compromise between penetration capability and surface roughness sensitivity, and is therefore often the preferred frequency when it comes to discriminating between different sea ice types (Hong and Yang, 2018).

2.6 Speckle

Speckle is an inherent characteristic of all coherent imaging systems, including SAR. It is caused by the fact that each resolution cell consists of many separate targets that are too small to be individually resolved by the radar beam. As a result, the waves scattered from the many targets in each resolution cell will add coherently, resulting in a single vector that represents the amplitude and

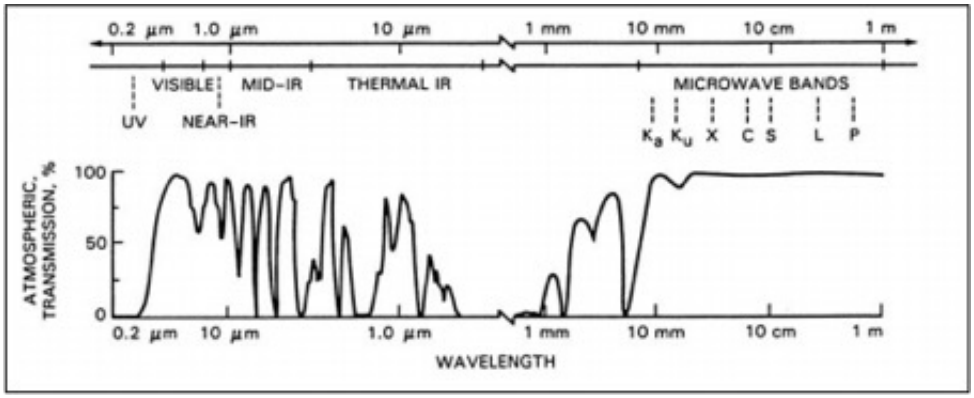

Figure 2.3: Atmospheric transmission for different wavelengths. Figure from (Henderson and Lewis, 1998)

phase of the signal. This process results in

- Constructive interference when features are reinforced, resulting in white pixels.
- Destructive interference when features are supressed, resulting in black pixels.

The result is an unwanted "salt and pepper" pattern over the image, which may reduce the effectiveness of target detection and image classification (Campbell and Wynne, 2011). Speckle is therefore something we want to remove.

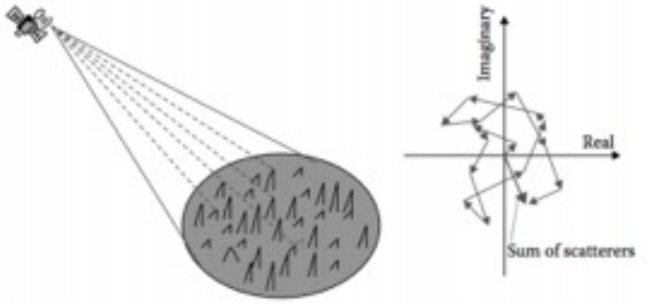

Figure 2.4: Speckle. Figure from (Lee and Pottier, 2009)

However, speckle is not considered as noise in the classical sense, but is rather an intrinsic part of the signal that also carries information. Speckle can consequently not be removed by e.g. increasing the transmission energy. One can, however, reduce the effect of speckle either by multi-looking, which means splitting the radar beam up into several parts and averaging them, or by spatial filtering, which means replacing the pixel value with an average over a

neighbourhood of pixels. The cost is, however, lower spatial resolution.

2.7 Polarization

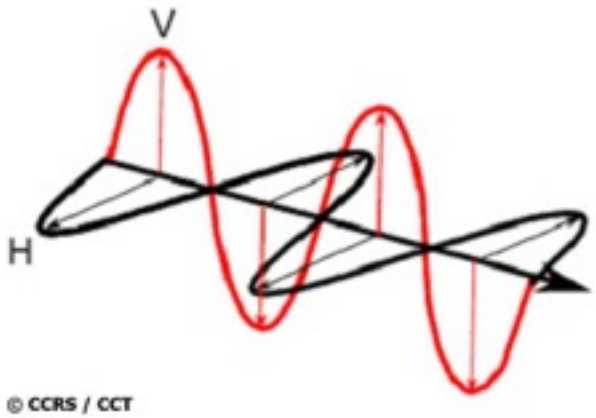

Figure 2.5: Horizontally polarized wave in black and vertically polarized wave in red. Figure from Canada Centre for Mapping and Earth Observation.

Electromagnetic waves are by Maxwell's equations described as synchronized oscillations of electric and magnetic fields propagating through space at the speed of light. The two fields will, in a homogenous and isotropic media, oscillate perpendicular to each other and to the direction of propagation. The polarization of an EM wave denotes the orientation of the electric field of the EM wave (Campbell and Wynne, 2011). SAR systems were originally designed to transmit waves at either horizontal (H) or vertical (V) polarization and receive at either horizontal or vertical polarization. Recent years, however, some SAR systems have been developed to transmit and receive at different polarizations by switching between each pulse. This gives the opportunity to use the following configurations:

- HH – horizontal transmit and horizontal receive
- VV - vertical transmit and vertical receive
- HV – horizontal transmit and vertical receive
- VH – vertical transmit and horizontal receive

The first two channels are referred to as "co-polarized", as they have the same polarization. Oppositely, the two last is referred to as "cross-polarized" channels.

Radar systems can be split into three polarization groups. The first one is single polarization, which offers one of the co-polarized channels. The second is dual polarization, which offers either the combinations (HH,HV) or (VV,VH). The last one is quad polarization, which offers all four polarization modes, albeit with a lower swath width than single- and dual polarization. Dual- and quad polarization enables the user to measure polarization properties of the surface in addition to the amplitude that can be measured from single polarization. Since surface targets have unique polarization signatures in the same way that they have unique spectral signatures, the type of polarization used will influence the signature of the returned signal. Dual- and quad polarization products can therefore give a deeper understanding about the complex scattering mechanism between the radar pulse and the target, and hence provide more accurate detection and classification of surface features than single polarization.

2.8 Scattering

Any interface separating two media with different EM properties will affect an EM wave incident on it (Elachi and Van Zyl, 2006). Usually the incident wave is dispersed into different directions after interaction with a medium, a process referred to as scattering. How the incident wave is scattered depends on many factors, including physical size and orientation of the target, incidence angle, polarization, dielectric properties of the target, and the surface roughness relative to the wavelength of the incident wave (Elachi and Van Zyl, 2006).

The most important quantity for a SAR system is the intensity of the return signal. Amongst other things, this quantity is dependent on the surface roughness. Higher roughness results in greater intensity on the return signal. Whether a surface appears smooth or rough depends on the wavelength of the radar signal. The roughness can be statistically described by its standard deviation around the mean flat surface (Elachi and Van Zyl, 2006). The most used criterion to describe the roughness of a surface is the Rayleigh criterion, given as

$$s_h \geqslant \frac{\lambda}{8} cos(\lambda_i) \quad (11)$$

where s_h is the standard deviation in surface height, λ is the wavelength and θ is the incidence angle. The criterion states that a surface is rough if this inequality holds. The criterion implies that a surface looks rougher when illuminated with shorter wavelengths or smaller incidence angles.

Scattering can be divided into three main types; surface scattering, double-bounce scattering and volume scattering. Having a basic understanding of

these three scattering mechanisms is of great importance when working with SAR images, as different sea ice types and water are subject to different scattering mechanisms. Hence, the use of information about different scattering mechanisms can be used to discriminate between different ice types and water.

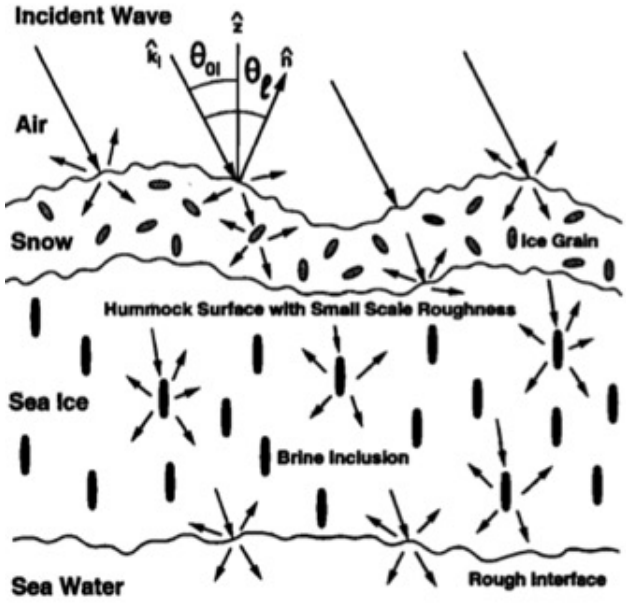

Figure 2.6: Surface scattering off the ice surface and volume scattering within the ice. Figure obtained from(Nghiem et al., 1995)

Surface scattering

Surface scattering occurs when the incident wave is dispersed only once, and is strongest in the co-pol channels (Cloude, 2010). It typically occurs between two homogenous media, such as between air and ocean, when the surface is relatively flat compared to the wavelength of the incident wave. The scattering is then primarily a function of the surface roughness and water content of the medium - the higher the water content, the higher the reflectivity. Usually, a smooth target will appear dark in the SAR, as most of the radiation is scattered in the specular direction (as long as it not is directly oriented towards the sensor) (Moen et al., 2013). Oppositely, rough targets appear bright, as some of the radiation is scattered back to the sensor.

Double-bounce scattering

Double-bounce scattering is a type of scattering that occurs when the incident wave is dispersed twice in the interaction process. This is typically caused by dihedral corners, that can be found in buildings or ice edges. Targets that are subject to double-bounce scattering usually appear very bright, as the majority of the incident energy is directed back to the sensor.

Volume scattering

Volume scattering occurs when the transmitted wave penetrates into the target where brine inclusions and cavities gives multiple random scattering (Moen et al., 2013). This often occurs in multi-year ice, due to the volume geometry. Penetration depth into the medium is inversely proportional to the radar wavelength.

2.9 Scattering matrix

When the incident wave from a SAR system interacts with a scattering surface, the characteristics of the surface can be obtained from a backscattering matrix. For a quad-polarimetric system, a 2x2 matrix of complex scattering coefficients S_{xx} is produced for each pixel. This is referred to as the Scattering matrix, or Sinclair matrix, $\mathbf{S}$, and relates the incident electric field E^i, referred to as the Jones vector, to the scattered electric field E^s by

$$\begin{bmatrix} E_x^s \\ E_y^s \end{bmatrix} = \frac{e^{-jkR}}{R} \begin{bmatrix} S_{HH} & S_{VH} \\ S_{HV} & S_{VV} \end{bmatrix} \begin{bmatrix} E_x^i \\ E_y^i \end{bmatrix} \quad (12)$$

where k denotes the wave number and R is the distance between the sensor and the target (Fors et al., 2016). The scattering matrix is then given as

$$\mathbf{S} = \begin{bmatrix} S_{HH} & S_{VH} \\ S_{HV} & S_{VV} \end{bmatrix} = \begin{bmatrix} \left|S_{HH}e^{j\phi HH}\right| & \left|S_{VH}e^{j\phi VH}\right| \\ \left|S_{HV}e^{j\phi HV}\right| & \left|S_{VV}e^{j\phi VV}\right| \end{bmatrix} \quad (13)$$

where $|S_{xx}|$ is the amplitude and ϕ_{xx} the phase of the complex scattering coefficients (Fors et al., 2016). For dual-pol systems, however, the scattering matrix is reduced to a 2x1 Lexicographic vector, given as

$$\mathbf{S} = \begin{bmatrix} S_{HH} \\ S_{HV} \end{bmatrix} = \begin{bmatrix} \left|S_{HH}e^{j\phi HH}\right| \\ \left|S_{HV}e^{j\phi HV}\right| \end{bmatrix} \quad (14)$$

The outer product of this vector is defined as the covariance matrix

$$\mathbf{C} = \frac{1}{L}\sum_{i=1}^{L} \mathbf{s}_i \mathbf{s}_i^{*T} \quad (15)$$

where L is the number of scattering vectors, s_i is the SLC vector for each pixel i and $*T$ is the Hermitian transpose (Fors et al., 2016). **C** can then be expressed as

$$\mathbf{C} = \begin{bmatrix} \langle S_{HH}S_{HH}^* \rangle & \langle S_{HH}S_{HV}^* \rangle \\ \langle S_{HV}S_{HH}^* \rangle & \langle S_{HV}S_{HV}^* \rangle \end{bmatrix} \quad (16)$$

where $\langle \cdot \rangle$ is the ensemble averaging and $*$ denotes the complex conjugate. Since the amplitude is related to the intensity via the equation

$$I = A^2 \quad (17)$$

means that, since $\langle S_{HH}S_{HH}^* \rangle = I_{HH}$ and $\langle S_{HV}S_{HV}^* \rangle = I_{HV}$ when d=2, the covariance matrix can be expressed as

$$\mathbf{C} = \begin{bmatrix} I_{HH} & (S_{HH}S_{HV}^*)^2 \\ (S_{HV}S_{HH}^*)^2 & I_{HV} \end{bmatrix} \quad (18)$$

For many applications, one assume that HH and HV are uncorrelated, hence $(S_{HH}S_{HV}^*)^2 = (S_{HV}S_{HH}^*)^2 = 0$. However, a part of this thesis is to investigate whether these elements could contain any valuable information for ice-water separation, and they are therefore assumed to be non-zero in this thesis.

2.10 TOPSAR

The Terrain Observation with Progressive Scans SAR (TOPSAR) technique is used to achieve wide swath coverage, and is utilized by Sentinel-1 on the interferometric wide swath mode and extra wide swath mode. This method acquires images by steering the beam both in range direction and backward to forward in the azimuth direction for each burst (Veci, 2015). TOPSAR is superior to the old ScanSAR method, as it achieves the same resolution and coverage, but with a more uniform signal-to-nose ratio (SNR) and distributed target ambiguity ratio (DTAR) (Veci, 2015). Sentinel-1 EW SLC products consists of one image per sub-swath for each polarization, for a total of ten images per product, where each sub-swath is processed as a separate SLC image. Mosaic operation is then required to merge together the sub-swaths into one image. This can create "seams" between each subswath, which is particularly noticeable in cross-pol over dark areas.

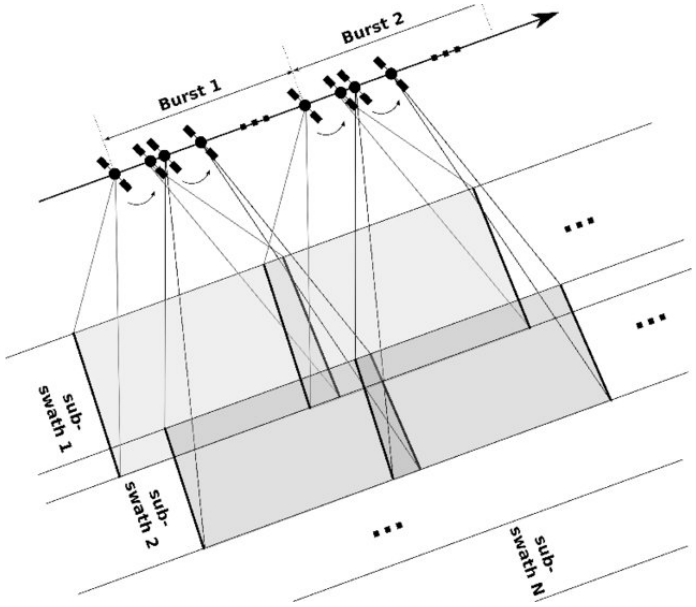

Figure 2.7: TOPSAR scanning geometry. Figure obtained from (Park et al., 2017).

3

SAR measurement of Arctic sea ice

This chapter discusses the SAR measurements of sea ice. The purpose is to give a brief introduction to the underlying physics that makes it possible to use active microwave sensors to obtain information about sea ice and water from satellites. This includes a brief introduction to sea ice, including its dielectric properties.

3.1 Introduction to sea ice

Between 11 and 15 % of the Earth's surface is covered by sea ice (Onstott, 1992). Sea ice is a mix of frozen water, liquid brine inclusions, solid salts, microalgae, trace elements, gases and other impurities (Hunke et al., 2011), and is formed when the sea surface is cooled to a temperature of about -1.8C, given that the water has a salinity of about 33 ppt (Onstott and Shuchman, 2004).

Sea ice goes through different stages of development during its formation, with the rate of ice growth being highest in the beginning and slowing down as it increases in thickness. Sea ice can take many different forms depending on temperature and wind conditions. The World Meteorological Organization has defined a common nomenclature of sea ice based on its age and thickness.

These classes are (Krokan, 2018):

New ice

New ice is a common denomination on recently formed sea ice. This type of ice consists of ice crystals that is weakly frozen together, and has a distinct form only when floating. New ice can be splitted into several subclasses based on its stage of development:

Under calm conditions, the uppermost part of the sea water will freeze into a very thin and smooth ice layer. in presence of wind and waves, the thin layer will suspend into the water and form frazil ice. If wind and waves persists, the frazil ice will further coagulate into a soupy layer called grease ice, and after a while, clumps called shuga will form. When the shuga has grown to a thickness of about 1 cm, it will harden into what is referred to as pancake ice.

Nilas ice

When sea ice is formed under persisting quiescent conditions, it is characterized according to its visual properties, which also is directly related to its thickness.

Nilas ice has a matt surface and is up to 10 cm in thickness. It is described by its thin, elastic crust which easily is bended on waves. Subdivisions includes dark nilas, which is under 5 cm and very dark in color, and light nilas, which is more than 5 cm and is bright in color.

Young ice

Young ice, with a thickness of 10-30 cm, is described as ice in the transition stage between nilas and first-year ice. Subdivisions includes grey ice from 10 to 15 cm, and grey-white ice from 15-30 cm.

First-year ice

Sea ice that is thicker than 30 cm and not more than one winter's growth is referred to as firstyear ice. It typically has a thickness up to 2 meters, and may be subdivided into thin first-year ice from 30-70 cm, medium first-year ice from 70-120 cm and thick first-year ice over 120 cm.

Multi-year ice

Ice that has survived a summer melt season is known as multi-year ice, and has typically a thickness ranging from 2 to 4 meters, with ridges up to 20 meters

(O'Connell, 2011). Multiyear ice can also be distinguished from first-year ice by its lower salt content and its thicker snow cover (typically 0.4m for MYI and 0.1m for FYI).

3.2 Electromagnetic properties of sea ice and ocean

A SAR signal is scattered off the sea ice either by surface or volume scattering (Dierking, 2013). The relative contribution from each of the scattering mechanisms is highly dependent on the relative permittivity (ϵ) of the medium, describing its dielectrical properties, and is defined as

$$\epsilon = \epsilon' + j\epsilon'' \quad (19)$$

where the real part ϵ' characterizes how easy the incident wave penetrates into the medium, and the imaginary part $j\epsilon''$ describes the electromagnetic loss of the material (Onstott and Shuchman, 2004). Typically, the bigger the dielectric constant, the less is the penetration, and stronger is the backscattering, resulting in a brighter feature in the SAR image.

The relative permittivity and loss of water is high, typically $\epsilon' > 40$ and $\epsilon'' > 4$ due to the high polarity of water molecules (Onstott and Shuchman, 2004). However, when sea water freezes, the permittivity is considerably reduced, as frozen water do not have the same rotational possibility as liquid water. Sea ice will typically have values for ϵ' of 3 to 5, and $j\epsilon''$ of 0.1 to 1.0 (Onstott and Shuchman, 2004).

3.3 Backscatter of sea ice and ocean

Even though images generated by SAR's can look similar to those generated by passive optical systems, the principals behind these two acquisition methods are completely different. An optical system is using a lens or mirror system to steer radiation from the ground onto a two-dimensional array of detectors. The angular relationship is then maintained between two targets on the ground and on the image. The received signal for an optical system is mainly a function of

1) Solar illumination
2) Atmospheric attenuation

3) The interaction mechanism between the radiation and the surface, which is on a molecular level, i.e. vibrational and electronical energy transitions.

SAR systems, on the other side, "sees" the surface in a fundamentally different way than optical sensors. SAR systems use the time-lag between the echoes backscattered from different targets to separate them from each other in range direction, and the Doppler history to separate them in the azimuth direction. The received signal for a SAR system is, according to (Onstott and Shuchman, 2004), a function of

1) Polarization
2) Frequency
3) Incidence angle
4) Scattering characteristics of the illuminated area. This includes physical ice properties such as salinity, temperature, surface roughness, surface inclination, snow layers and presence of water (Sandven et al., 2006).

SAR backscatter of sea ice

Sea ice is predominantly subject to two types of scattering; surface- and volume scattering (Dierking, 2013). Typically, both types occur simultaneously, but depending on surface properties, one of them can be negligible compared to the other. Smooth surfaces, such as newly formed ice (nilas or young ice) are mainly dominated by specular reflection, and will therefore appear dark in the SAR images. However, the growth of small scale surface features, such as frost flowers, can significantly increase the backscatter intensity over ice (Dierking, 2013). Backscatter values are also highly dependent on topographic features like ridges. A surface inclined towards the radar will give a strong return signal.

Volume scattering occurs if some of the incident wave is transmitted into the sea ice and redirected back and forth by volume inclusions up to the surface again. Volume inclusions, such as air bubbles and brine pockets, are found in multi-year ice, but can also occur in younger ice (Dierking, 2013). However, the volume scattering is reduced if the surface is wet due to melting at higher temperatures, as melt-water may penetrate the volume inclusions and re-freeze (Dierking, 2013).

SAR backscatter of ocean

The penetration of SAR microwaves in ocean is typically only a few millimetres into the topmost layer, due to high absorption and scattering losses. The use of SAR imaging of the ocean is therefore limited to the ocean surface and the immediate subsurface (Elachi and Van Zyl, 2006). SAR is in particular

sensitive to the small (mm to cm-scale) wind-induced surface waves with the same wavelength of the incoming signal, called Bragg waves. When these waves match the projection of the transmitted microwave onto the local ocean surface, wavefronts scattered from different portions will be in phase and add constructively, resulting in a strong backscatter signal (Onstott and Shuchman, 2004).

The backscattered signal of ocean is a function of the wavelength, orientation, and the tilt of the waves compared to the SAR. For calm ocean, the surface will be generally smooth and specular reflection away from the sensor will dominate. Rough sea, on the other hand, will result in increased backscatter as more energy is reflected back to the sensor.

Under influence of higher winds, ocean can appear as bright or even brighter than sea ice at co-polarisation, while it remains dark at cross-polarisation. Ice-water separation under such conditions are therefore easier at cross-polarisation (Dierking, 2013).

The choice of polarization also plays a role. Ocean clutter is typically more suppressed at HH than VV (Hong and Yang, 2018). HH is therefore better suited for measuring ocean. Anyhow, using Sentinel-1, HH/HV is also usually the only available polarization over the Arctic, as Sentinel-1 is usually preprogrammed to this mode over this area.

Separating sea ice and ocean in SAR images

Sea ice appear different than ocean in SAR images because they have different backscatter signature. In particular, sea ice typically gives stronger return signal than water. However, there are several factors that can disturb image interpretation in SAR images, which then again can cause sea ice to be classified as water and vice versa. The main reasons are:

1) **Speckle**. This phenomena is discussed in 2.5. High amount of speckle implies lower radiometric resolution and thus lower ice-water separability.

2) **Thermal noise**. Additive thermal noise in the HV channel in TOPSAR images varies in both range and azimuth and includes three main features: burstwise variation (scalloping), elevation angle-dependent range variation and discontinuities between subswaths (Park et al., 2017). Thermal noise can be characterized as white noise, that is, with symmetric Gaussian distribution with constant spectral density for all bandwidths and zero mean (Freeman, 1993). Thermal noise is seldom a problem in co-polarization bands, as the backscatter intensity is strong enough to screen the variations in thermal noise.

In cross-polarization bands, however, thermal noise can be a serious problem, as backscatter generally is much weaker (Park et al., 2017). This is particularly a problem over water, where the return signal usually is extra weak. The result is a noise floor throughout the image where any signal below this floor not will be distinguishable from the thermal noise level (Onstott, 1992). Some of the thermal noise can, however, be removed from SLC images by using the "thermal nosie removal" function in Sentinel Application Platform, but the result is loss of phase information.

3) **Incidence angle dependency**. Operational sea ice charting require wide swath imagery. Sentinel-1 EW images covers about 400 km in range direction, and are thus acquired over a broad range of incidence angles (from 19 °to 47 °). The incidence angle affects the interaction between the incident microwave and the surface, producing a decay in backscatter intensity from near- to far range which disturbs image interpretation and classification (Doulgeris and Cristea, 2018). This intensity decay, which is much stronger in co-pol than cross-pol, is usually greater than the between-class variation (Doulgeris and Cristea, 2018). This can result in segmentation of homogenous classes along the range direction. The decay rate is typically different for different terrain types. Usually, the decay rate is much steeper for water than for sea ice. An incidence angle correction should therefore, ideally, take this into account, that is, applying different incidence angle correction for different terrain types.

4) **Variable and changing surface conditions**. Another problem is the overlap in backscatter intensity of ice and water, as both classes can take a broad range of values depending on many factors. For example can high winds cause open water to give a strong backscatter signal similar to sea ice. Oppositely can exceptionally smooth sea ice act as specular scatterers and thus look similar to ocean.

In order to separate sea ice and water correctly, these four problems must be taken care of. Generally, speckle is reduced though multi-looking, thermal noise is reduced by pre-processing techniques or increasing the transmission power and the effect of incidence angle is reduced by different incidence angle corrections. The variable and changing surface conditions are hard to deal with, but adding extra features may improve the separation.

4

Data and area of interest

4.1 Sentinel-1

The Sentinel-1 satellite constellation consist of two polar orbiting SAR satellites working in the same orbit 180 degrees' phase shifted to each other. The satellites are operating in C-band with the capability to acquire data in (HH, HV) or (VV,VH) polarization. Each satellite has a repeat cycle of 12 days; hence the constellation repeats it's orbit in 6 days, but more frequent the higher the latitude. Sentinel-1 utilizes four different acquisition modes; stripmap (SM), wave mode (WV), interferometric wide swath (IW) and extra wide swath (EW). Images can be downloaded for free at scihub.copernicus.eu. These images are available either as single-look complex (SLC) or ground-range detected (GRD) images.

Single-look complex products (SLC)

SLC images consist of a series of burst focused SAR data, provided in the slant range by azimuth imaging plane. The data has been geo-referenced using orbit and altitude data from the satellite. Each pixel in the image is represented as a complex number that contains both phase information and the magnitude of the backscattered signal. The SLC products are processed to obtain a single look in both dimensions, using the full available signal bandwidth (Bourbigot et al., 2016). SLC resolution varies from near to far range due to the incidence angle and the slant geometry, but is constant in range for each sub swath.

Ground-range, multi-looked, detected products (GRD)

GRD images consists of focused SAR data, lying in the ground range by azimuth surface. The data has been detected, multi-looked and converted to ground range by an Earth ellipsoid model. The result of multi-looking is that speckle is reduced, but at the cost of lower spatial resolution. Phase information is also lost through multi-looking. Each pixel is represented by the detected magnitude.

Type	Resolution	Pixel spacing	Number of looks	ENL
SLC	7.9x43 to 15x43 m	5.9x19.9 m	1x1	1
GRD	93x87 m	40x40 m	6x2	10.7

Table 4.1: SLC vs GRD

The pixel spacing for SLC above is given in slant range. In range direction, however, the pixel spacing corresponds to swath width divided by number of of pixels in range. Hence, roughly 400 km divided by approximately 40 000 pixels, which is equal to about 10 m. Thus, pixel spacing is $\sim 10x20$ m in range x azimuth.

4.2 Study area

The area is located in the Barents sea, south-east of Svalbard. At the time of the year of which the image is acquired, that is, the end of the winter, Arctic sea ice is at its maximum extent. During winter and spring, the ice edge is often located in this area. This is therefore a particularly relevant area for ice-water classification, as fishing vessels, oil installations and tourism are dependent on reliable ice maps when going into these waters.

Figure 4.1: Area of interest

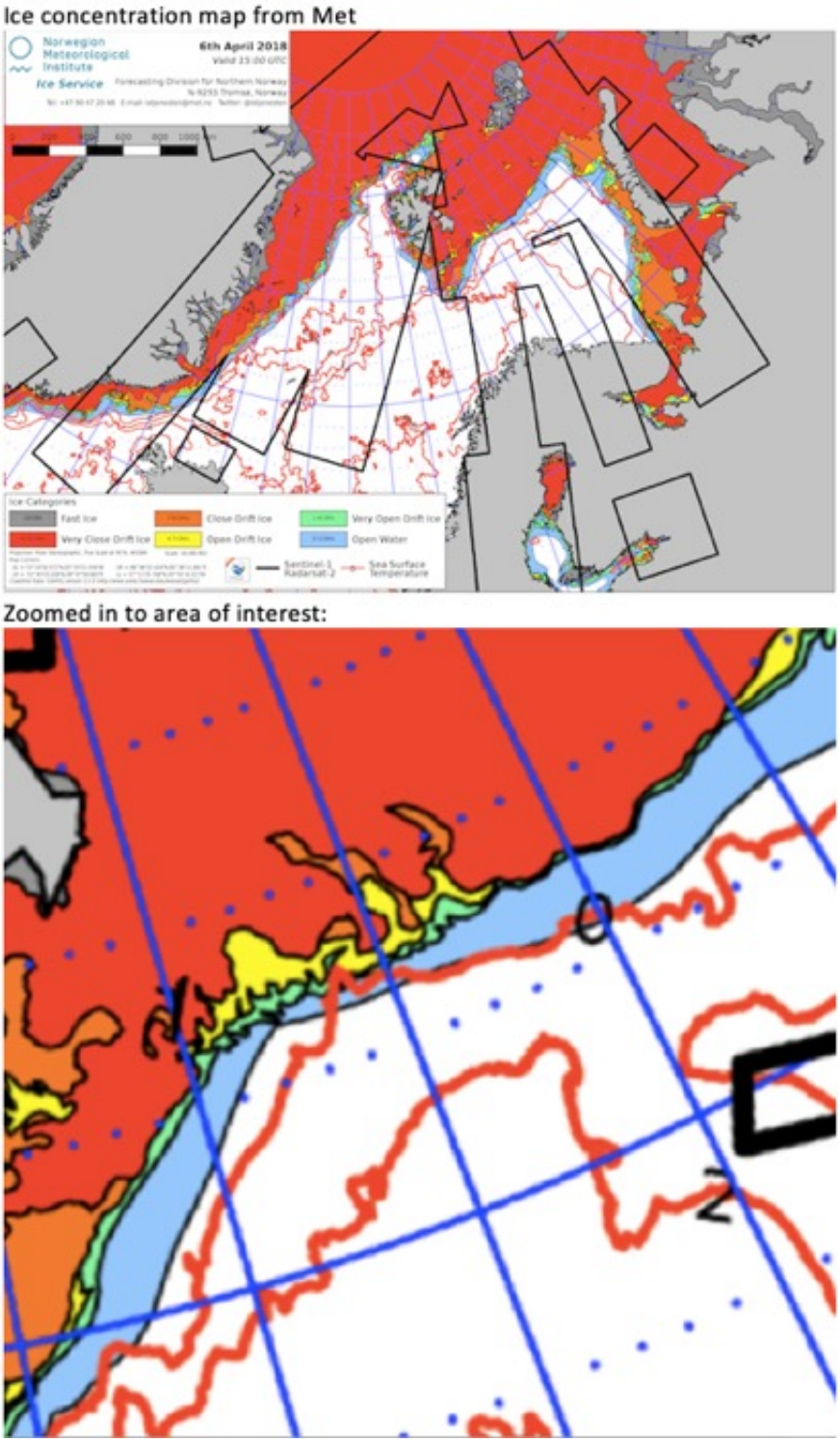

Figure 4.2: Ice concentration map from the Norwegian meteorological institute over the study area

4.3 Data

An extra wide, Sentinel-1 SLC image, acquired 6. April 2018 05:09:55, was download from Copernicus. This scene was found to be especially useful for this project, as it comprised water and sea ice over all incidence angles. This makes it easy to obtain the incidence angle decay for both sea ice and water over all incidence angles. Is also seems to consists of both calm, smooth water close to the ice edge and rougher water further out, in addition to different types of sea ice. From yr.no, the temperature at Longyearbyen for that particular day was measured to -13.5 °C. Even though this is some distance away from the study area, we assume that similar conditions are here, that is, cold temperatures and no melting.

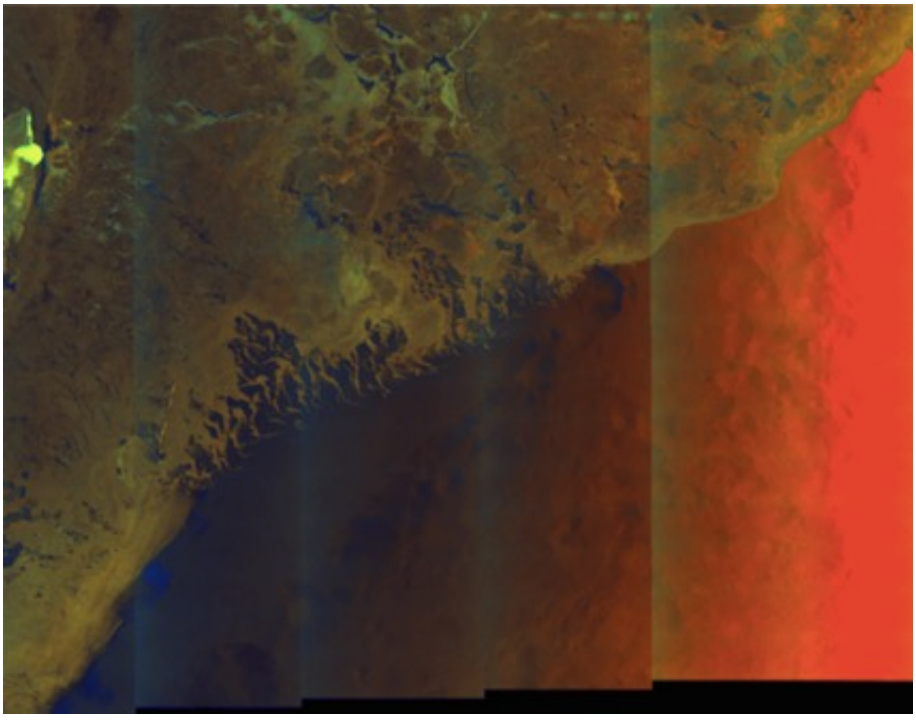

Figure 4.3: The image showed "in colors", where red=HH intensity, green=HV intensity and blue=0

5 Method

In this section, the method used in this project is described. This includes the pre-processing steps, the segmentation and labelling part, the accuracy calculation and the production of ice-concentration maps.

5.1 Pre-processing

Some pre-processing steps have to be carried out before working with the images. These were performed using the Sentinel Application Platform (SNAP) developed by ESA, and included radiometric calibration and de-bursting (merging the subswaths together). It is also common to include a noise removal step in SNAP, but this was omitted as it also removes phase information. Multi-looking was performed using MATLAB, and resulted in multi-look complex (MLC) data in covariance matrix format. All features were extracted from this matrix.

5.1.1 Radiometric calibration

The power of the backscattered signal that a SAR sensor receives is not limited to the interaction of the transmitted signal with the target only, but also accounts for factors such as the antenna gain, system loss and effective aperture of the signal. This introduces a radiometric bias in the signal, which makes it

inadequate for quantitative use of SAR data (El-Darymli et al., 2014).

The intention of radiometric calibration is to convert the pixel values in the SAR image from the biased backscattered signal to being represented by the Radar Cross Section (RCS) and the backscatter coefficient, which is directly related to the backscatter of the scene. This step is necessary when comparing data from different sensors, or data from the same sensor that has been acquired under different conditions.

Sentinel-1 images come with Look up tables (LUT) that allows for three calibrations: σ_0, β_o and γ_0. The calibration used in this thesis is σ_0, and gives the RCS per unit area in the ground-range direction. β_o is the RCS per unit area in the slant range, and is known as the radar brightness coefficient. γ_0 is the RCS per unit area in the incident wavefront, that is, perpendicular to the slant-range (El-Darymli et al., 2014).

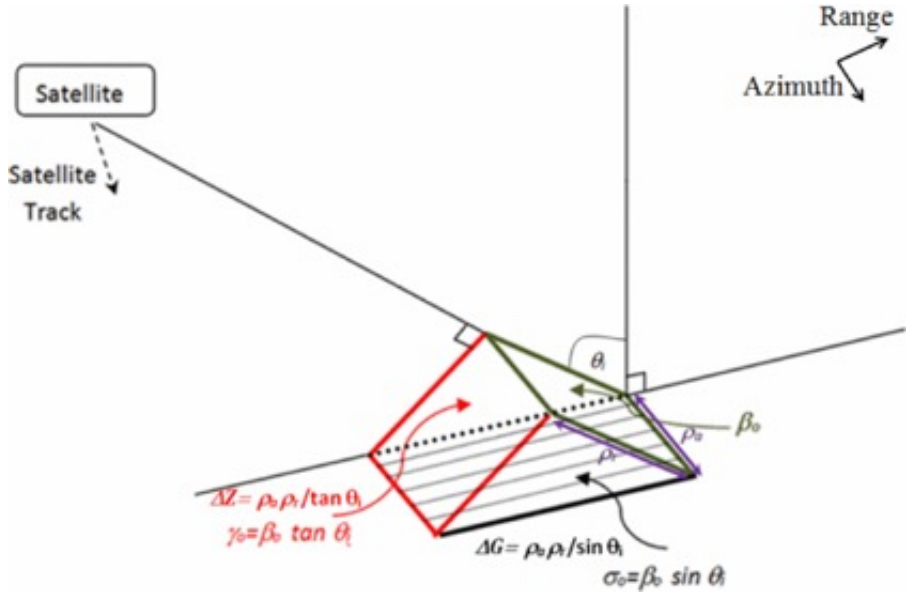

Figure 5.1: Shows the relationship between the three calibration coefficients. Figure from (El-Darymli et al., 2014)

5.1.2 Multi-looking

Multi-looking is performed by using a sliding window technique to replace each pixel value with the average value of the window being slided over. The purpose is to reduce speckle, and thus increase the radiometric resolution, i.e. the separability between each class. In other words, we want to reduce the within-class variation such that there is less overlap between classes. There is,

however, a trade-off between radiometric and spatial resolution. Multi-looking has a blurring effect, as smaller targets is mixed up in the smoothing process, and spatial resolution will therefore decrease with number of looks.

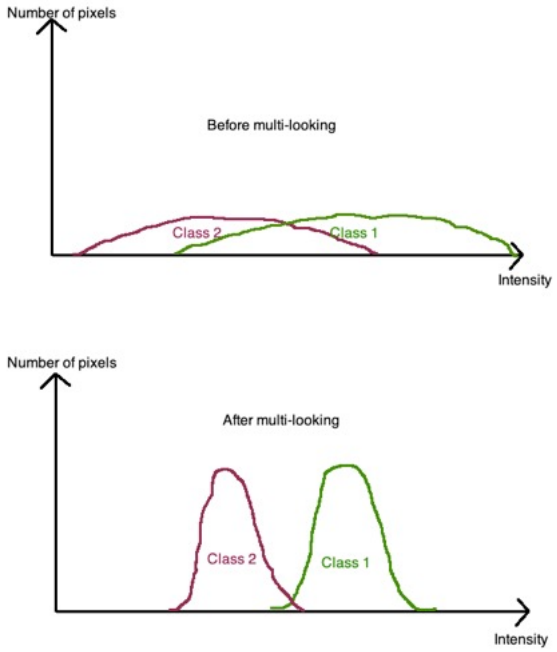

Figure 5.2: The effect of multi-looking

5.1.3 Log-transformation

Logarithm transformation is applied to all features except EPF5. The purpose is to spread out the data such that distinct classes are visible. This step is often necessary in order to separate classes from each other.

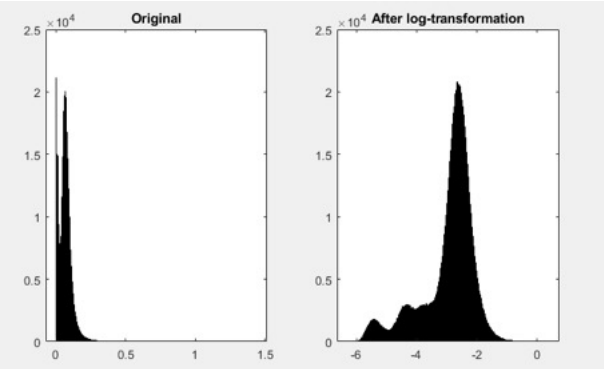

Figure 5.3: The effect of log-transformation

5.2 Feature extraction

A set of 7 features is used in this project. All are extracted from the covariance matrix

$$\mathbf{C} = \begin{bmatrix} \langle S_{HH}S_{HH}^* \rangle & \langle S_{HH}S_{HV}^* \rangle \\ \langle S_{HV}S_{HH}^* \rangle & \langle S_{HV}S_{HV}^* \rangle \end{bmatrix}$$

An overview of the features is presented in table 5.1.

	Feature	**Type**
MLI1	HH intensity	Single-channel intensity
MLI2	HV intensity	Single-channel intensity
EPF1	Geometric brightness	Polarimetric
EPF2	Cross-polarization ratio	Polarimetric
EPF3	Relative kurtosis	Statistical
EPF4	HH-HV correlation magnitude	Polarimetric
EPF5	HH-HV correlation angle	Polarimetric

Table 5.1: Features used in this project

5.2.1 Intensity features

The single-channel intensities I_{HH} and I_{HV} are based on one backscatter intensity only. They are found in the diagonal elements in the covariance matrix (Fors et al., 2016), and is defined as

$$I_{HH} = \langle |S_{HH}|^2 \rangle$$
$$I_{HV} = \langle |S_{HV}|^2 \rangle$$

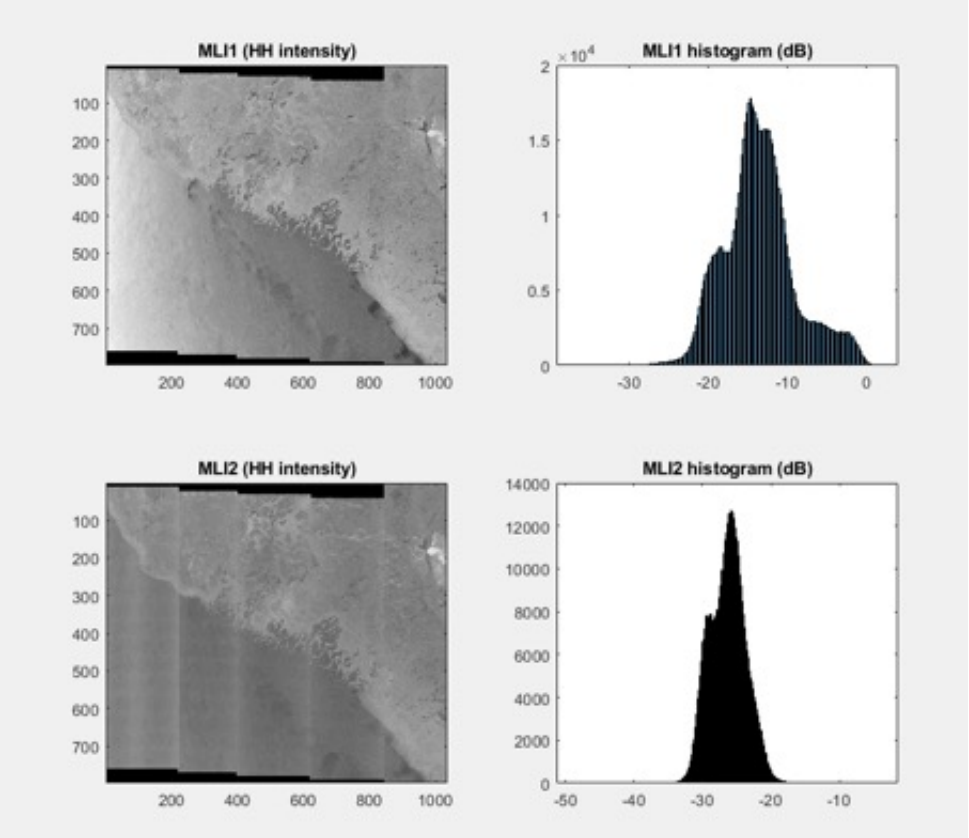

Figure 5.4: Multi-looked intensities (MLI) and their histograms

5.2.2 Polarimetric features

Polarimetric features combine information from two or more channels, i.e. it requires dual- or quad-pol data. Polarimetric features can characterize the polarimetric signature of sea ice and water. This enables improved physical interpretation of the scattering properties of the targets. Of the 7 features, we have defined EPF 1, 2, 4 and 5 as polarimetric features, while EPF3 is defined as a statistical feature, as it can be derived from single-channel data. The polarimetric features are:

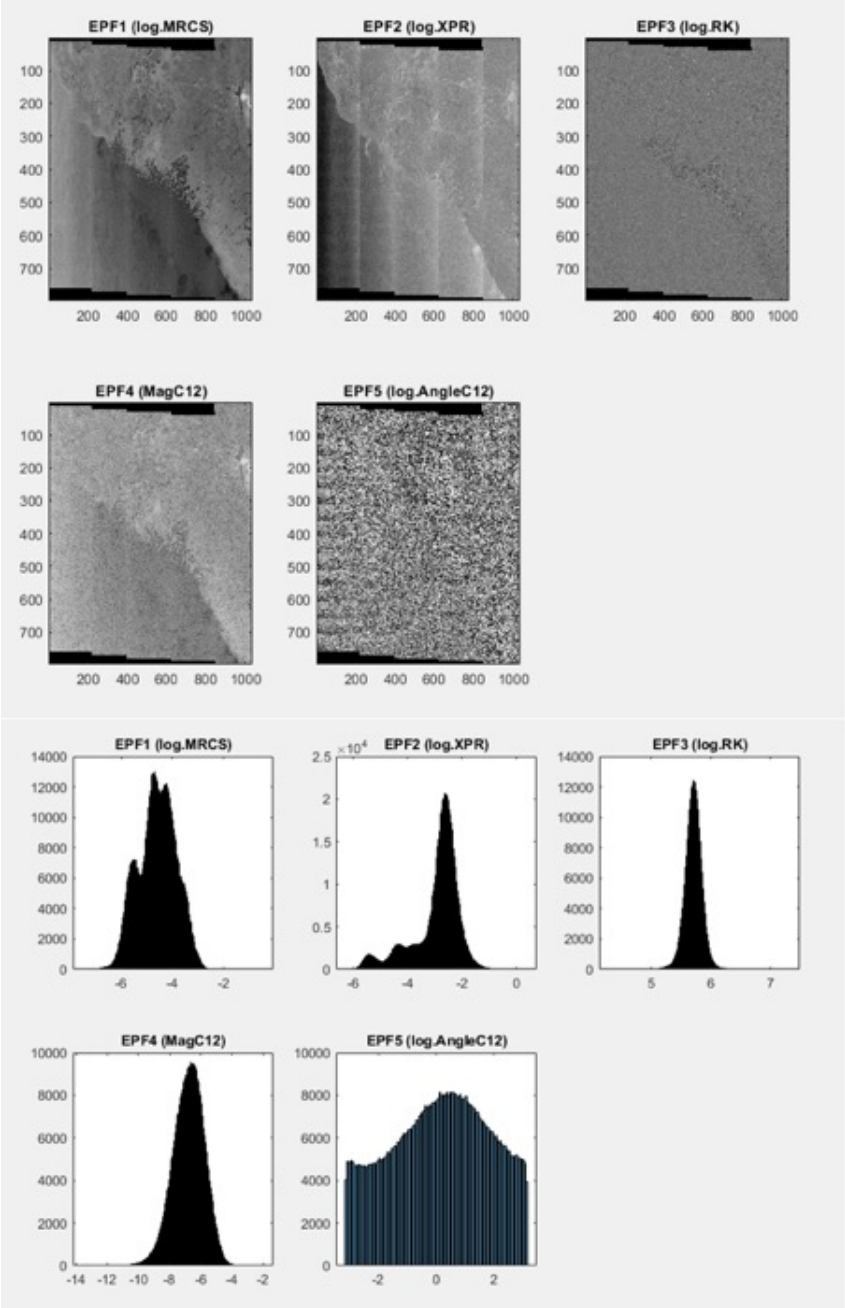

Figure 5.5: Extended polarimetric features (EPFS) and their histograms

Geometric brightness

The geometric brightness represents the total multi-variate intensity (Moen et al., 2013), or the total power received by the two channels, and is given

as

$$B = \sqrt[d]{det(\mathrm{C})}$$

where d is the dimensionality of the input, hence 2 for dual-pol, and C is the covariance matrix. The span, i.e. the sum of the two intensities, could in theory be used instead of the determinant, and presumably give similar, or possibly, even better results. However, only the determinant was tested in this thesis, due to time constraints.

Cross-polarization ratio

The cross-pol ratio is given as

$$R_{cr} = \frac{\langle S_{HV} S_{HV}^* \rangle}{B}$$

In our case with d=2, it will be equal to $R_{cr} = \frac{I_{HV}}{B}$. This feature provide a relative measure of volume scattering versus surface scattering (Lubin and Massom, 2006). It is considered to be useful for discriminating between ice types and determining ice age (Moen et al., 2013).

HH-HV correlation magnitude

The magnitude of the correlation between HH and HV is defined as

$$|\rho| = \left| \langle S_{HH} S_{HV}^* \rangle \right|$$

This feature's ability to discriminate between ice and water is not found much information about in the literature.

HH-HV correlation angle

The HH-HV correlation angle is defined as

$$\angle\rho = \angle(\langle S_{HH} S_{HV}^* \rangle)$$

and represents the phase difference between HH and HV channels. This feature is not found much information about neither. Phase difference could however, in theory, be used for discriminating between surface and volume scattering.

5.2.3 Statistical feature

Relative kurtosis

Relative kurtosis (RK) is defined as

$$RK = \frac{1}{L}\frac{1}{d(d+1)}\sum_{i=1}^{L}\left[s_i^{*T}C^{-1}s_i\right]$$

and is a measure of non-gaussanity, that is, how equal the data distribution is to a Gaussian distribution. For Gaussian data, the RK is equal to 1. Data with high kurtosis is associated with a sharp peak, quick drop and heavy tails (Moen et al., 2013). Large values of RK are likely for deformed ice and inhomogeneous areas (Fors et al., 2016). RK can be calculated both for single-pol and multi-pol.

5.3 Segmentation

The segmentation was done using an unsupervised feature-based mixture of Gaussian segmentation algorithm, developed by Anthony Paul Doulgeris at CIRFA. This model integrates the incidence angle dependency into the probability density function, and thus manages to account for the incidence angle variation that occurs in wide swath SAR images. By doing it this way, instead of as a global pre-processing correction method, one can account for the incidence angle decay for each class, and thus get a more precise correction.

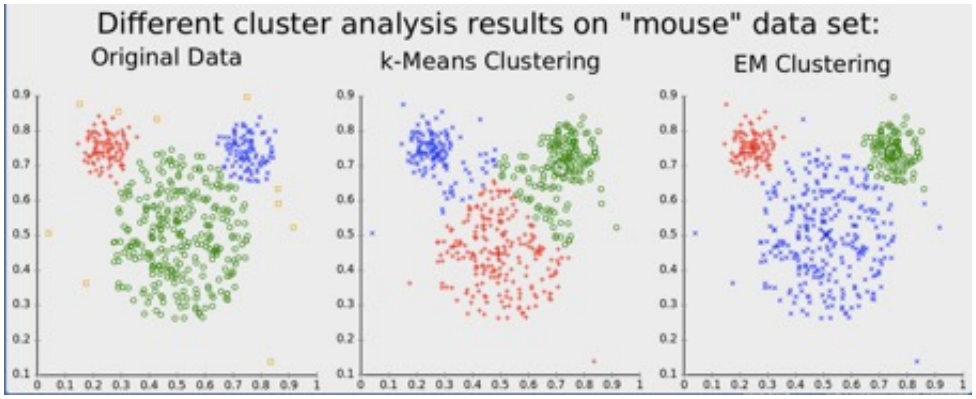

Figure 5.6: K-means vs Mixture of Gaussian. Image from (Wikipedia contributors, 2019)

A mixture of Gaussian model is superior to segmentation models such as k-means, because it takes the variance into consideration. In k-mean clustering,

one assumes that the data is spherical. This hard assignment might often lead to misclassification (see figure 5.6), as it assumes equal class variations, which is not the case for sea ice and water. While k-means finds k to minimize $(x - \mu_k)^2$, a Gaussian mixture use expectation maximization to find k to minimize $\frac{(x-\mu_k)^2}{\sigma^2}$. In other words, in cases were there is uncertainty about the data and which class they belong, mixture of Gaussian is often a good clustering algorithm.

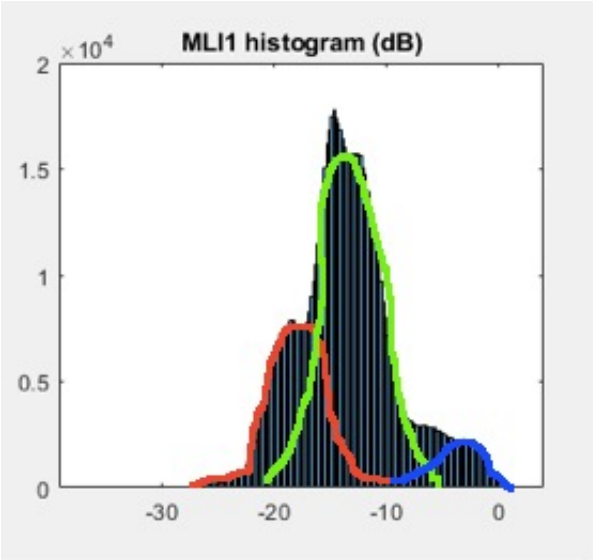

Figure 5.7: HH intensity histogram for our data indicates three natural Gaussian distributed classes. Mixture of Gaussian segmentation is therefore expected to work fine.

Doulgeris' mixture of Gaussian model assumes that all data points in the data set belong to a mixture of a fixed number of Gaussian distributions along constant incidence angle azimuth lines (Doulgeris and Cristea, 2018). The mean values can then be expressed as a linear function of the incidence angle: $a_k + b_k\theta$, where a_k is the interception, b_k is the slope and θ the incidence angle. When including the class weights π_k and this linear function, the probability density function is given as:

$$p_{X,\theta}(x,\theta) = \sum_{k=1}^{M} \pi_k \frac{1}{(2\pi)^{d/2} \mid \Sigma \mid^{1/2}} e^{-\frac{1}{2}(x-(a_k+b_k\theta))^T \Sigma^{-1}(x-(a_k+b_k\theta))}$$

Hence, each class is a function of three parameters: covariance Σ_k, slope b_k and intersection a_k. The parameters can be estimated using the Expectation-

Maximization equations:

$$a_k = \frac{\sum_{i=1}^{n} z_{ik} x_i - b_k \sum_{i=1}^{n} z_{ik} \theta_i}{\sum_{i=1}^{n} z_{ik}}$$

$$b_k = \frac{\sum_{i=1}^{n} z_{ik} \theta_i x_i - a_k \sum_{i=1}^{n} z_{ik} \theta_i}{\sum_{i=1}^{n} z_{ik} \theta_i^2}$$

$$\Sigma_k = \frac{\sum_{i=1}^{n} z_{ik} (x_i - (a_k + b_k \theta_i))(x_i - (a_k + b_k \theta_i))^T}{\sum_{i=1}^{n} z_{ik}}$$

Where z_{ik} is the membership weights.

After segmentation, a Markov Random Field (MRF) smoothing method is applied to the segmented image. This is done in order to to make the classes look more homogeneous, which simplifies the interpretation of the classified image (Doulgeris, 2013).

5.4 Labelling

The segmentation algorithm used in thesis clusters the image into different regions based on the distribution of the pixel values. It does not, however, give any physical meaning to the different classes, i.e. telling what each class actually is. The purpose of this thesis is to do ice-water classification. Hence, each class in the segmented image must be assigned to either water or sea ice.

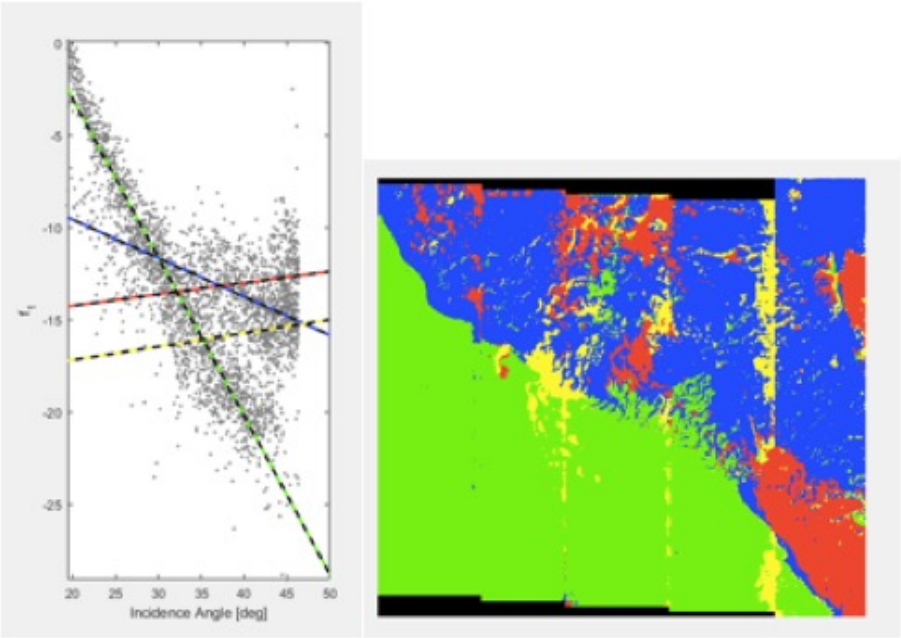

Figure 5.8: Right: Segmented image based on HH and HV intensity. Left: HH intensity as function of incidence angle of the segmented image.

The segmentation algorithm used in this thesis outputs the pixel values of each segmented class as a function of incidence angle, example shown in figure 5.8. It also outputs the slope of each class. Since we know that slope of HH intensity is much steeper for water than for sea ice, this property can be used to determine whether each class is water or sea ice.

Inspecting the HH intensity slope of different classes for different images, it was clear that the slope usually was between -0.8 and -0.10 db/1° for water, and between +0.1 and -0.3 db/1° for sea ice. Thus, by setting a threshold somewhere between these values, classes are labelled as water if the slope is steeper than this threshold, or else it is sea ice. In this project, different thresholds were investigated, but -0.6 db/1° worked fine most of the time.

5.5 Accuracy assessment

An accuracy assessment was performed on the classification results, as we wanted a quantitative score on how good the classification was, not only visual inspection.

A ground truth image was made by manually selecting homogeneous areas of either sea ice and water on the SAR image, using the roipoly function in MATLAB. Most of the ocean was selected, and four areas within the ice that seemed to contain sea ice only. Ideally, optical images should have been used for validation, but this was omitted due to time constraints.

The accuracy was then calculated by comparing the classified image with the ground truth pixel-to-pixel-wise, and simply counting the number of correctly classified pixels, using a for-loop in MATLAB, and then dividing the number of correctly classified pixels with the total number of pixels in the ground truth.

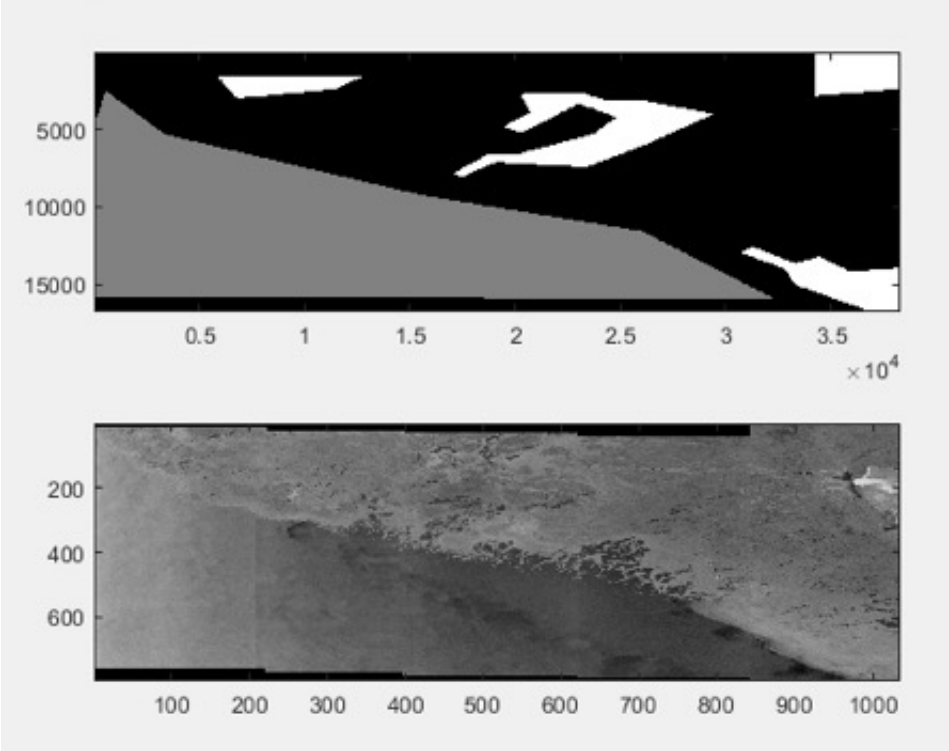

Figure 5.9: On top: Ground truth, where sea ice is white, water is grey. Compared with EPF1 on the bottom.

5.6 Ice concentration estimation

Sea ice concentration describes the relative amount of ice compared to some reference area. Ice concentration maps issued by national ice services is expressed in tenths of area coverage (Armstrong, 1972). Sea ice concentration is an important tool for navigators to determine potentially passable leads

and openings in the ice. It is also important in a scientific manner, as it helps determine a number of other important climate variables such as extent and volume. In this thesis, the ice concentration was calculated using a $12x12$ sliding window technique over the classified ice-water image. The ice concentration then corresponded to the fraction of ice pixels divided by total pixels in the window. Using the same scale and standard ice chart color code as the national ice service, the ice was classified as following

- **Open water** = 0-1/10 (white)
- **Very open drift ice** = 1-4/10 (blue)
- **Open drift ice** = 4-7/10 (turquoise)
- **Close drift ice** = 7-9/10 (green)
- **Very close drift ice** = 9-10/10 (yellow)
- **Fast ice** = 10/10 (red)

6

Results and discussion

This section consists of four parts. The first part is a feature evaluation, where the ability of the features described in section 5.2 to separate sea ice from water is evaluated. This is followed by an investigation of resolution in ice-water classification. Furthermore, it turned out that thermal noise was a big problem in the classified images. Therefore, a simple method to remove some of the thermal noise from EW SLC images is presented in the third part. Finally, ice concentration maps are created, based on the ice-water maps, and compared to the hand drawn ice concentration map from the meteorological institute for the same date and area.

6.1 Experiment 1: Feature selection

In this section, the ability of different combinations of features to discriminate between sea ice and water, is presented. These features are HH and HV intensity, geometric brightness, cross-pol ratio, relative kurtosis and magnitude and angle of the HH-HV correlation. First, the results of using intensity features only is presented. This is followed by a brief discussion on where we find misclassified pixels and what they are caused by. Furthermore, the results of using the extended polarimetric features is presented. The idea is that they will improve ice-water classification, and hence remove some of the misclassified pixels.

Classification is based on the image described in section 4.3. The scene is multi-looked with a 60x20 filter with a stepping size of 22x44 in azimuth and range, resulting in a spatial resolution of 930x870m with a pixel spacing of 440x440m, which is the same order of size as the hand drawn ice maps from met.

6.1.1 Classification based on single-channel intensities

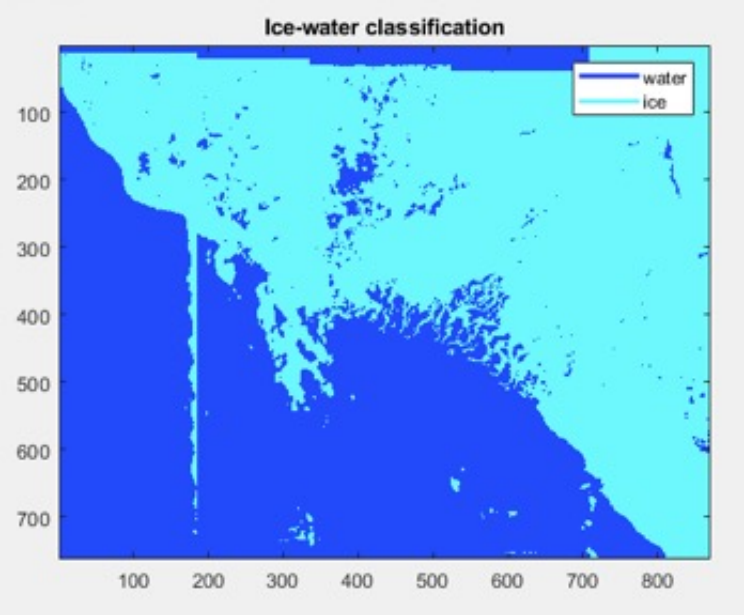

Figure 6.1: Ice-water classification based on both intensities

Total accuracy of the ice-water classifier using both single-channel intensities is 98.36 %, which is acceptable. There are, however, some misclassification, and by taking a look on the classified image, it is clear that three different phenomena causes the misclassification.

1) Thermal noise over water. The effect of thermal noise is much stronger over water, as the backscattered signal is much weaker then over sea ice. Thus, bright lines occurs between the swaths. The result is that the bright pixels is classified as sea ice instead of water.

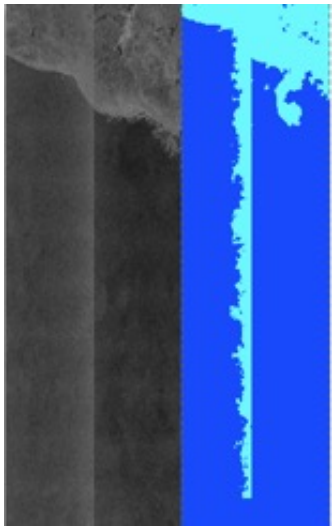

Figure 6.2: Misclassification due to thermal noise

2) Wind conditions over open water. In this case, an area that looks like smooth, quite open water, based on visual inspection of HH and HV intensity images, was misclassified as sea ice.

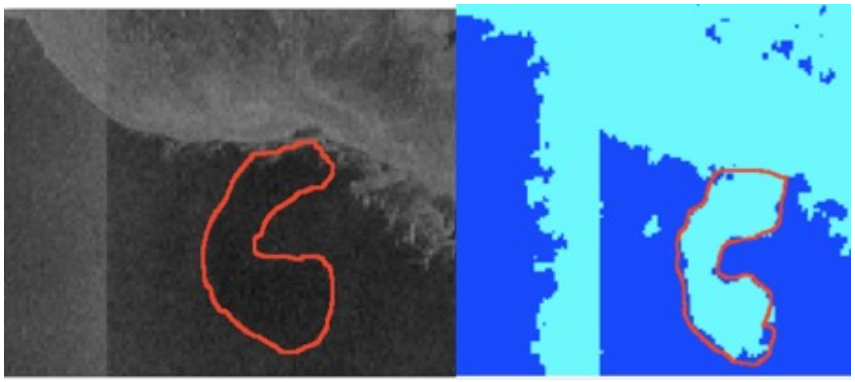

Figure 6.3: Water misclassified as sea ice due to wind conditions

3) Sea ice misclassified as water. This happened several places within the sea ice. In one case, illustrated in figure 6.3, some of the darker sea ice, located between bright sea ice, was misclassified as water.

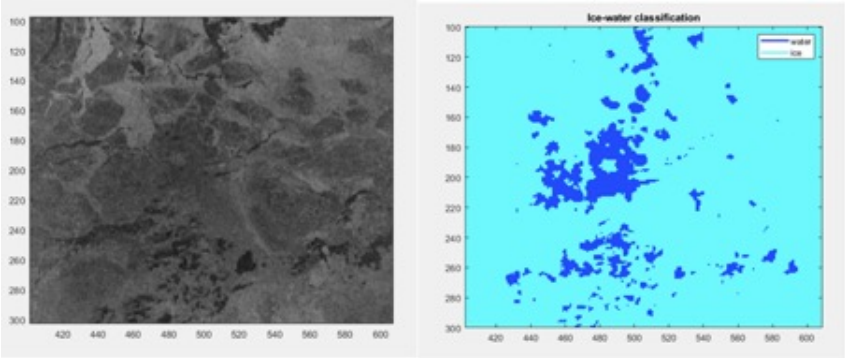

Figure 6.4: Darker sea ice surrounded by bright ice is misclassified as water

6.1.2 Classification based on EPF 1 and EPF 2

Total accuracy of the ice-water classifier using EPF 1 (Geometric brightness) and EPF 2 (Cross-polarization ratio) was 97.31 %. Hence, accuracy was lower than using intensities. Seemingly, misclassification due to thermal noise is a bigger problem using EPF 1 and EPF 2 than using the intensity features. From visual inspection, this appears to be the main reason of why the accuracy is lower. Apart from that, the results are rather similar.

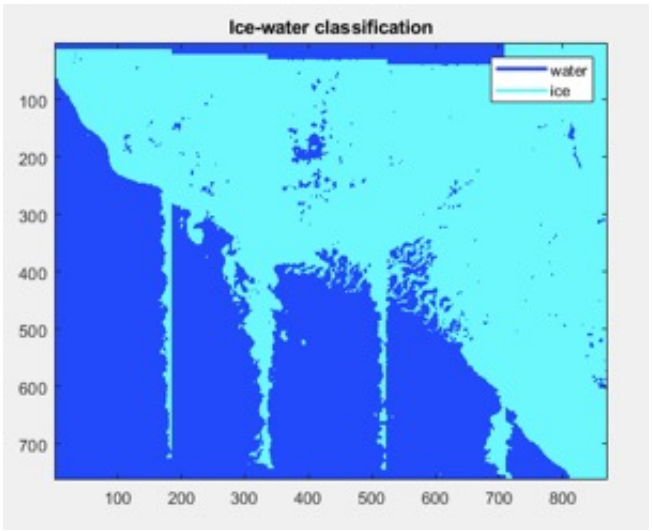

Figure 6.5: Ice-water classification using EPF 1 and EPF 2 (Geometric brightness and cross-pol ratio

6.1.3 Classification based on EPF1, EPF2 and EPF3

By also using EPF3 (relative kurtosis) together with EPF1 and EPF2, the accuracy increased from 97.31 % to 99.29 %. Hence, a solid improvement. The apparent reason is that a majority of the misclassified pixels between the swaths, probably related to thermal noise, now are classified correctly. Apart from some misclassified pixels between swath 1 and 2, the image looks more or less correctly classified over both sea ice and ocean.

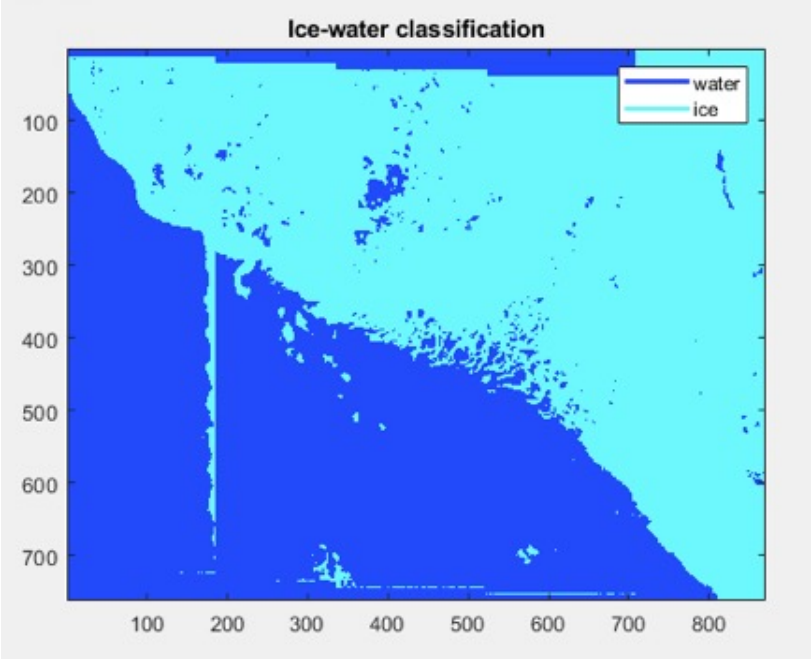

Figure 6.6: Ice-water classification based on EPF 1, 2 and 3

6.1.4 Classification based on EPF 4 and EPF 5

The classification results based on magnitude and angle of HH-HV correlation, alone and together, are presented below. The magnitude (EPF 4) gives reasonably good separation between ice and water, except for swath 1, which is more or less completely classified as ice. Presumably, omitting swath 1, using all other four swaths could give decent results. The angle (EPF 5), on the other hand, seems to consists mainly of random noise, and does not tend to give any good separation between ice and water.

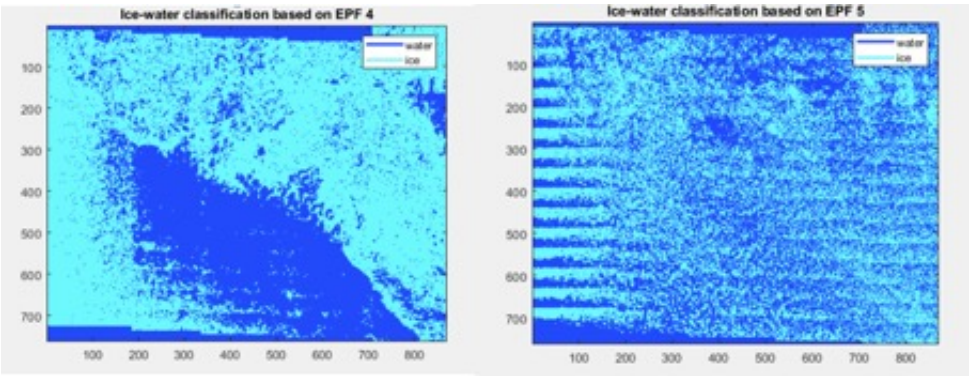

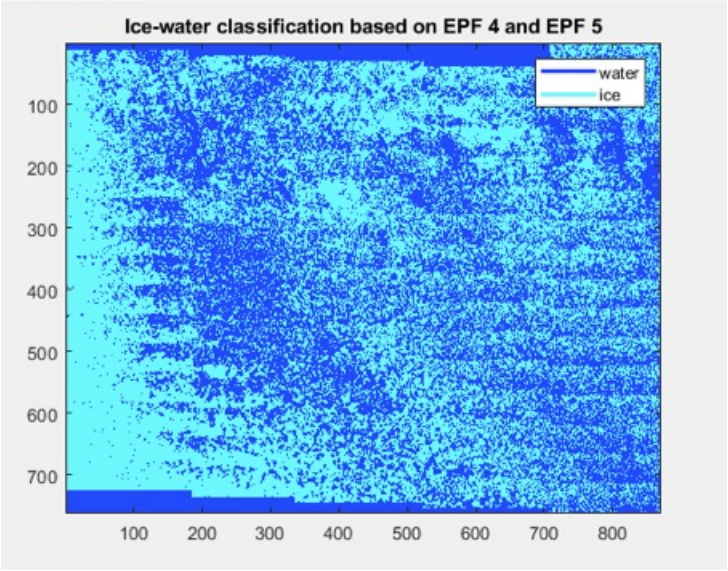

Figure 6.7: On top: Ice-water classification based on EPF 4 and 5, respectively. Bottom: On EPF 4 and EPF 5 together.

6.1.5 Classification based on EPF1, EPF2, EPF3, EPF4 and EPF5

The ice-water classification using all five EPF's have an accuracy of 99.27 %. In other words, almost the same as using EPF 1, 2 and 3. Hence, adding EPF 4 and 5 does not tend to have any big impact on the classified result. The use of EPF 4 and 5 does, however, due to the random nature of EPF 5, introduce some new noise. The noise is not a big problem in the classified ice-water image. It is, however, highly visible in the segmented image, as shown in figure 6.9.

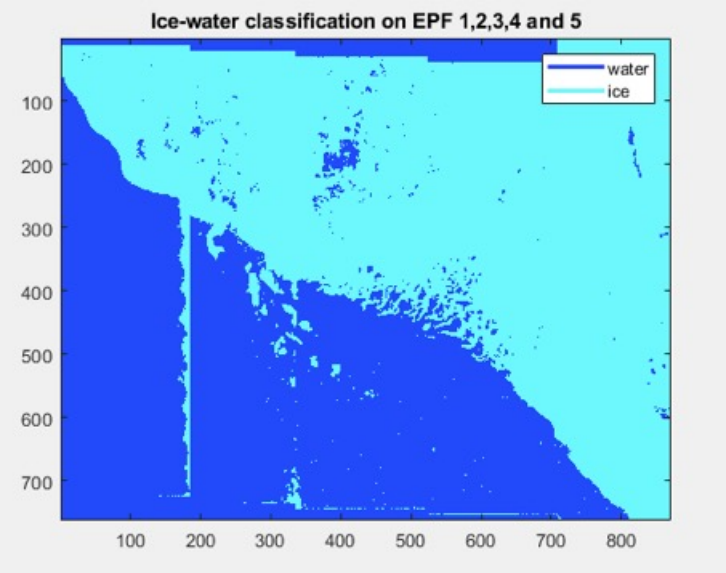

Figure 6.8: Ice-water classification based on all EPF's

The segmentation results:

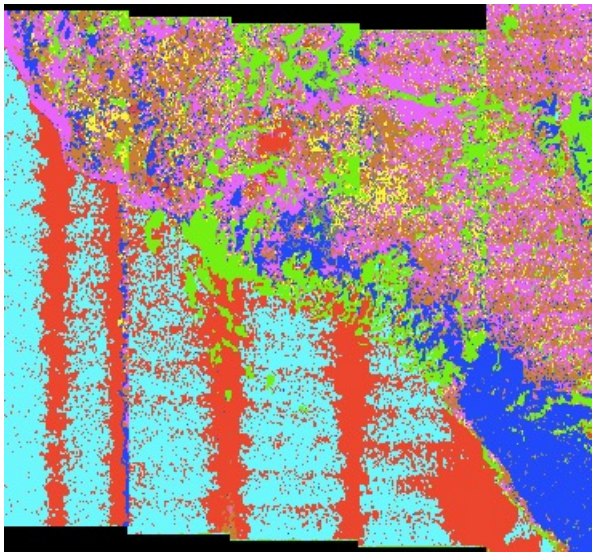

Figure 6.9: Segmentation results based on all EPF's

6.1.6 Results

Features	Ice-water classification accuracy
MLI 1 (HH)	93.45 %
MLI 2 (HV)	90.66 %
MLI 1 (HH) and MLI 2 (HV)	98.36 %
EPF 1	97.15 %
EPF 2	89.78 %
EPF 3	93.39 %
EPF 1 and EPF 2	97.31 %
EPF 1, EPF 2 and EPF 3	**99.29** %
EPF 1, EPF 2 and EPF 4	98.30 %
EPF 1, EPF 2 and EPF 5	98.14 %
EPF 1, EPF 2, EPF 4 and EPF 5	97.61 %
EPF 1, EPF 2, EPF 3 and EPF 4	98.62 %
EPF 1, EPF 2, EPF 3, EPF 4 and EPF 5	99.27 %

Table 6.1: Classification accuracy for different combinations of features

6.1.7 Concluding remarks of experiment 1

- In most cases, using two or more features at the time gives significantly higher classification accuracy than using only one feature as input.
- Ice-water classification on the intensities (MLI 1 and 2) gave slightly better results than using geometric brightness and cross-pol ratio (EPF 1 and 2), due to less thermal noise.
- Relative kurtosis (EPF 3) tend to increase the separability between ice and water and remove some of the thermal noise.
- Ice-water classification based solely on HH-HV correlation magnitude (EPF 4) suffers from noise in swath 1, but gives good ice-water separation if swath 1 is omitted.
- HH-HV correlation angle (EPF 5) does not contain any meaningful information when it comes to ice-water septation.
- The segmentation algorithm has several different hyper-parameters, such as number of looks, stepping size and sub-sampling, which needs to be tuned to obtain optimal performance of the classifier. Due to time constraints, these were only tested for a few values. Presumably, an even higher accuracy would be achieved by tuning these to the optimal values.

- Only the features ability to distinguish between ice and water is considered in this project. If the goal was to distinguish between ice types, different results are expected. EPF4, for instance, seems to have good separability between ice and water, but not necessarily between different ice types.

6.2 Experiment 2: Resolution investigation

The purpose of this experiment is to find the best achievable resolution on ice-water maps based on Sentinel-1 EW imagery, where noise not is a disturbing factor. The idea is to investigate whether it is possible to obtain ice-water maps with good enough resolution for tactical navigational use. This requires, in order to detect leads and cracks in the ice, a resolution in the order of 50-100 meter or better (Scheuchl et al., 2004). Such resolution is not achievable with GRD images (87x93m). Hence, a SLC image with 15x43 m resolution, the same as before, is used. The question is if the high resolution of SLC can be utilized, or if it has to be multi-looked down to the same resolution as GRD in order to remove speckle and increase the radiometric resolution enough to separate ice and water adequately. As illustrated in section 5.1.2, the overlap between classes is decreasing with number of looks. Hence, with few looks, the overlap between classes is expected to be significant, and lower classification accuracy is anticipated. In other words, spatial and radiometric resolution are inversely proportional. This is therefore a question of trade-off: how little can we multi-look and still achieve high enough radiometric resolution to discriminate ice and water in a satisfactory manner?

The experiment is conducted by multi-looking the previously used SLC image with various number of looks, and sub-sampling it to about half the pixel spacing of the spatial resolution. This is done in order to not lose information due to under-sampling (Nyquist). MLI 1 and 2 are used as features. Note: SLC images lies in the slant-range and has a spatial resolution of 8-15x43m from near- to far-range. The resolution varies in slant range but is constant in range direction for each swath. For GRD images, the resolution is 93x87 meters in range and azimuth, Thus, since the resolution using 6x2 looks is 93x87m in range, the resolution using 1x1 looks must be $\sim$ 93/6 x 87/2 $\approx$ 15x43 m. The spatial resolution is slightly different for each swath, but for simplicity's sake, 15x43m is assumed to be the resolution for the entire image in range and azimuth.

6.2.1 Results

Looks(1x1), stepping(1x1) = res(15x43m), pixel spacing(20x10m)

Without any smoothing or stepping, the classified images consisted only of one class. Hence, the classifier did not manage to separate ice from water at all. 15x43m resolution ice-water maps is thus not achievable, at least not with the segmentation algorithm used in this thesis.

Looks(3x1), stepping(1x2) = res(46x43m), pixel spacing(20x20m)

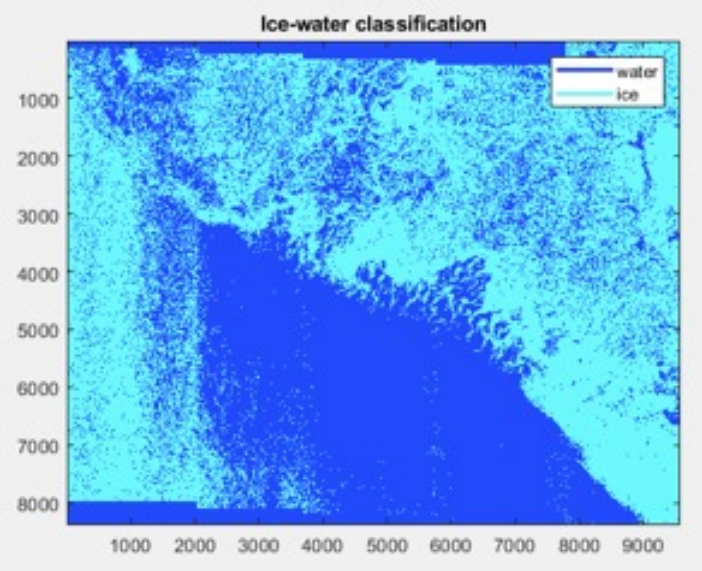

Figure 6.10: Ice water classification with resolution of 46x43 m

Classification on images with 46x43 meter gave an accuracy of 86.03 %. Since the radiometric resolution is pretty low with so few number of looks, there is still some overlap between sea ice and water. This is particularly a big problem in swath 1, where a lot of the water is classified as sea ice and vice versa. In the other four swaths, the classification result is better, although the noise is still a disturbing factor, especially over the sea ice. By excluding swath 1 from the classification, accuracy increases to 96.39 %, albeit with a reduction in coverage from 400 km to about 320 km. This reduction is, however, necessary if such resolution is wanted, as swath 1 is more or less useless.

Looks(6x2), stepping(2x4) = res(93x87m), pixel spacing(40x40m)

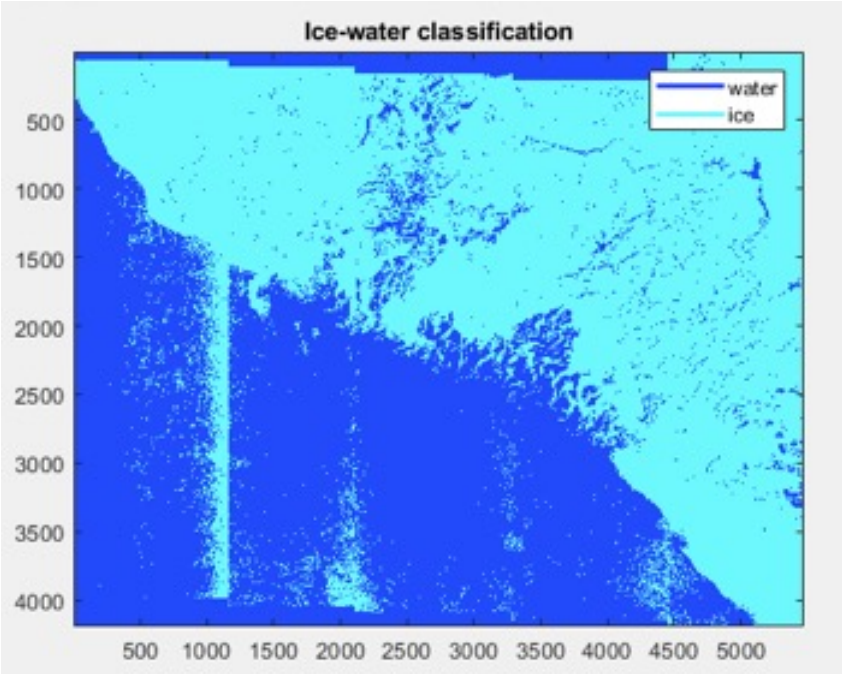

Figure 6.11: Ice water classification with resolution of 93x87 m

Classification accuracy with 93x87 meter resolution is 97.03 %, which is good. The noise also seems to be considerably reduced over sea ice. There is still some noise left in the first swath and in the transition between the other swaths. By excluding swath 1, the accuracy increases to 98.57 %. Presumably, by using some thermal noise removal technique, most of the misclassified pixels would have been removed, and the accuracy would be even higher.

Number of looks (azxrg)	Spatial resolution	Stepping	Pixel spacing	Accuracy of classifier	Accuracy omitting swath 1
3x1	46x43 m	1x2	20x20 m	86.03%	96.39%
6x2	93x87 m	2x4	40x40 m	97.03%	98.57%
12x4	186x194 m	4x8	80x80 m	97.29%	97.68%
18x6	279x264 m	7x14	140x140 m	97.53%	97.99%
36x12	558x516 m	14x28	280x280 m	97.64%	97.86%
60x20	930x870 m	22x44	440x440 m	98.33%	98.44%

Table 6.2: Classification accuracy for different resolutions

Looks(12x4), stepping(4x8) = res(186x194m), pixel spacing(80x80m)

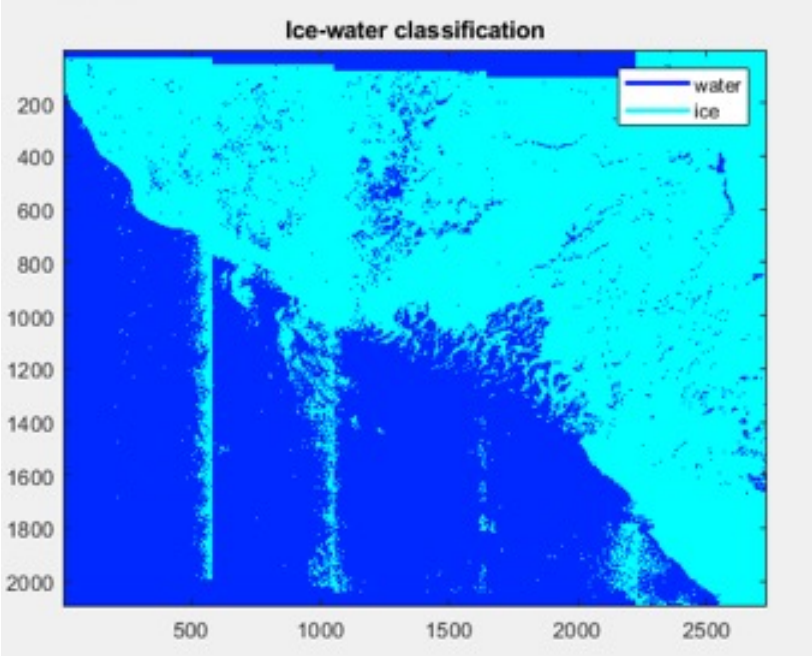

Figure 6.12: Ice water classification with resolution of 186x194 m

The accuracy with 186x194 meter resolution is 97.29 %, i.e. not that much better than the previous. There is some less misclassified pixels in swath 1. However, some new misclassification between swath 2 and 3 has arisen. For that reason, the accuracy without swath 1 is actually lower for this resolution than for 93x87 meter resolution.

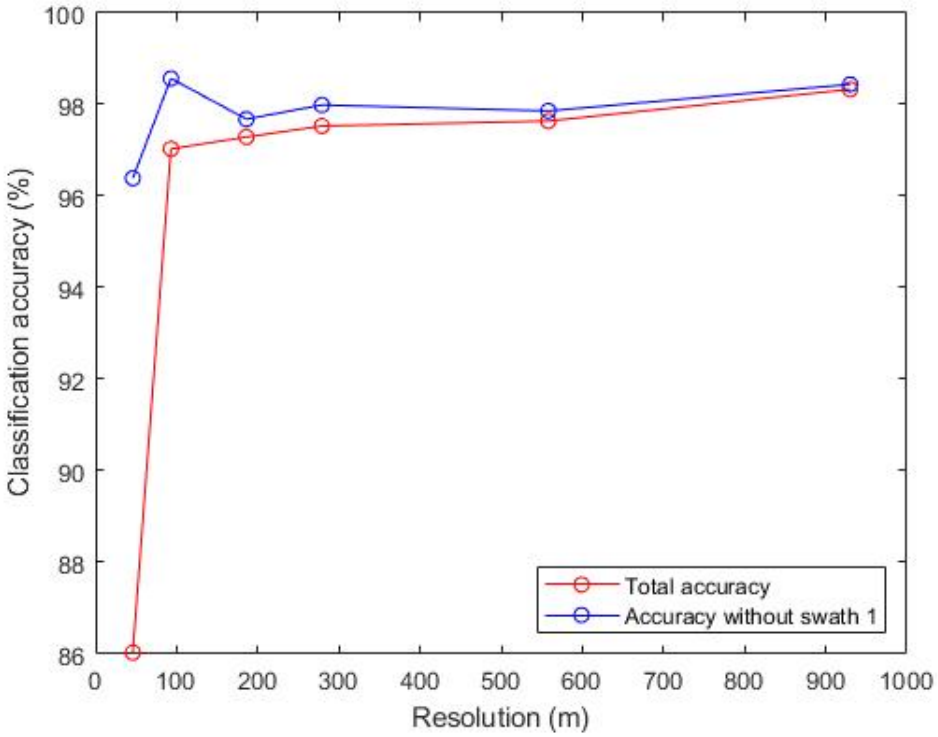

Figure 6.13: Ice-water classification accuracy as a function of azimuth resolution

6.2.2 Concluding remarks of experiment 2

- In most cases, but in particular for ice-water maps with high resolution, better accuracy is achieved by omitting swath 1. The cost is, however, that the coverage is significantly reduced.

- Classification directly on the SLC image, without any multi-look, is not possible, as all pixels are classified to the same class.

- It is possible to achieve ice-water maps with a resolution down to 46x43 meters. This can be obtained only from SLC images. The high resolution of these maps permits for detection of leads and cracks in the ice. The maps are, however, suffering from misclassification related to noise, especially in swath 1, which is more or less useless. By omitting this swath, quite high accuracy is achieved. The map is, however, possibly not reliably enough for tactical use, as the amount of speckle over the sea ice still is significant.

- $93x87m$ resolution ice-water maps seems like the best achievable reliable resolution. There is still some noise in these maps, but the majority of it could probably be removed by some thermal noise removal technique. These maps could be made using GRD, without any extra multi-look.

- Thus, if the requirement is a reliable ice-water map with full coverage, SLC is not necessary. The highest possible reliable resolution can be achieved from GRD.

6.3 Experiment 3: A proposed method for thermal noise removal over ocean in EW SLC images

Thermal noise accounts for the majority of misclassified pixels in the classified ice-water image. Hence, removing the thermal noise will significantly increase the classification accuracy. The noise varies along both range and azimuth direction throughout the HV intensity image. On the classified images, however, the effect of thermal noise is that water is misclassified as sea ice in the transition between the five swaths. Since thermal noise is additive, one can assume that the signal consist of two components; the actual signal component + the thermal noise component. Thus, by estimating the contribution of the thermal noise component and subtracting it from the signal, the actual signal component can be obtained. Since thermal noise only is a problem between the swaths in the classified image, that is, at the end of each swath in range direction, only this area needs to be considered. In particular, by inspecting the image, it turns out that the following incidence angles in the HV intensity image is disturbed by thermal noise:

- between 27.65 °and 28.51 °

- between 32.7 °and 34.3 °

- between 38.6 °and 39.05 °

- between 42.65 °and 43.38 °

The proposed thermal noise removal method works as follows:

- The area corrupted with thermal noise, that is, between the incidence angles described above, is located.

- The average of these pixels is then calculated for each line in range direction, for each of the four noise corrupted areas.
- Next, the average of the 10 neighbouring pixels to the noisy pixels is calculated for each line, for each of the four noise corrupted areas. The neighbouring pixels are considered as noise free.
- The noise component is then obtained by subtracting the noise free pixels from the noisy pixels.
- The final step is to subtract the noise from the noisy pixels.

Pseudo-code:

```
incAngleLeft = [27.65, 32.72, 38.63, 42.65];
incAngleRight = [28.51, 34.35, 39.05, 43.38];

image = HV intensity;

for j=1:4

  for i=all pixels in azimuth

        Noisy pixels = mean(image(i,(incAngleLeft(j):incAngleRight(j))));

        Normal pixels = mean(10 pixels next to noisy pixels);

        Noise = noisy pixels - normal pixels;

        Noise corrected pixels = noisy pixels - noise;
  end
end
```

6.3.1 Results

To demonstrate this, an ice-water classification based on MLI 1 and MLI 2 with $60x20$ multi-look and $22x44$ stepping, resulting in $930x870$ meter resolution with pixel spacing of $440x440$ meter is used.

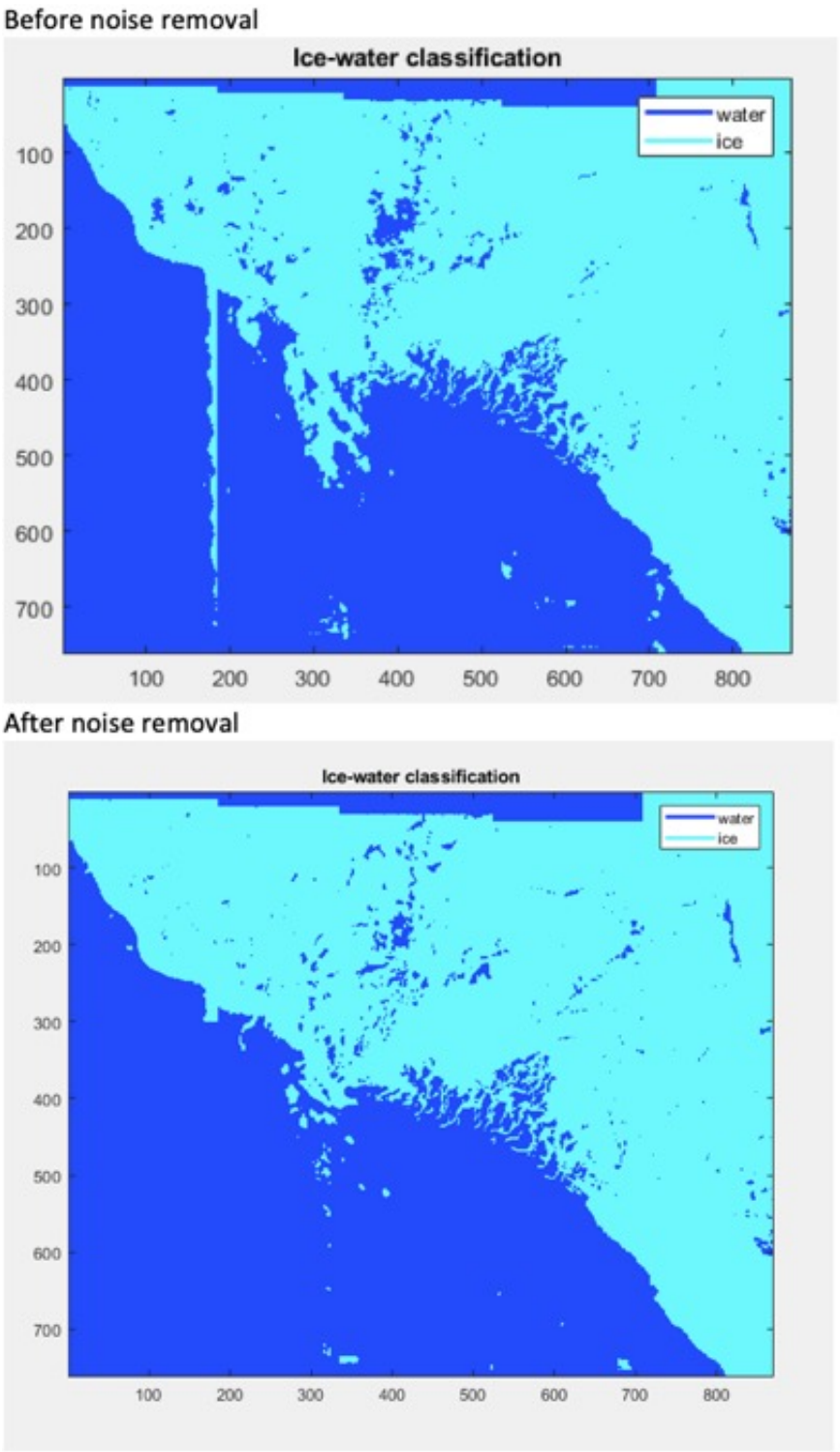

Figure 6.14: The effect of noise removal

6.3.2 Concluding remarks of experiment 3

- The accuracy increased from 98.33 % to 99.70 % using the described noise removal method. Still there is some noise left, but the result is much better.

- Presumably, this is a generic method and should work for all SLC images which is multi-looked to the same level, as the thermal noise supposedly is located in the same area in every image; i.e. at the end of each swath in range direction.

- The method was also applied to image with high resolution, but did not provide a satisfactory result. Probably because the noise is much more dominant and spread out over the swaths.

6.4 Experiment 4: Ice concentration maps

Tactical sea ice information products are needed, occasionally, to solve challenging tasks of navigation in the ice. The main users of this information are ships and icebreakers. Such information should be high resolution imagery, delivered as quickly as possible, preferably within a few hours after acquisition (Johannessen et al., 2006). Hence, there is no time for time-consuming hand drawing. In addition, the resolution of hand drawn maps is to low for tactical use. For that reason, tactical navigation is today mainly based on direct use of SAR images overlaid geographical coordinate grid (Johannessen et al., 2006). This requires that the navigator is trained in order to interpret the images correctly. However, as discussed in section 3.3, there are some challenges with direct interpretation of single-channel SAR intensities. Thus, derived ice information products, such as sea ice concentration, could in some cases be useful, and easier for the end-user to interpret. In the following section, two sea ice concentration maps, derived from the classified ice-water images, are presented; one with high resolution, meant for tactical navigation, and one with low resolution, meant for strategical navigation or scientific purposes. They are compared with the hand drawn maps from the Meteorological Institute to see if there is any difference.

6.4.1 Results

First, the high-resolution sea ice concentration map (93x87 m) is presented. Unfortunately, the thermal noise is strong for high-resolution imagery, and the proposed noise removal technique did not manage to remove it in this case.

The noise is therefore a big problem in this image.
As seen in figure 6.17, the high-resolution ice concentration map is able to pick up details such as leads in the ice that not can be seen in the hand drawn maps. These leads can be useful for ship navigation. However, the noise problem needs to be sorted out first.

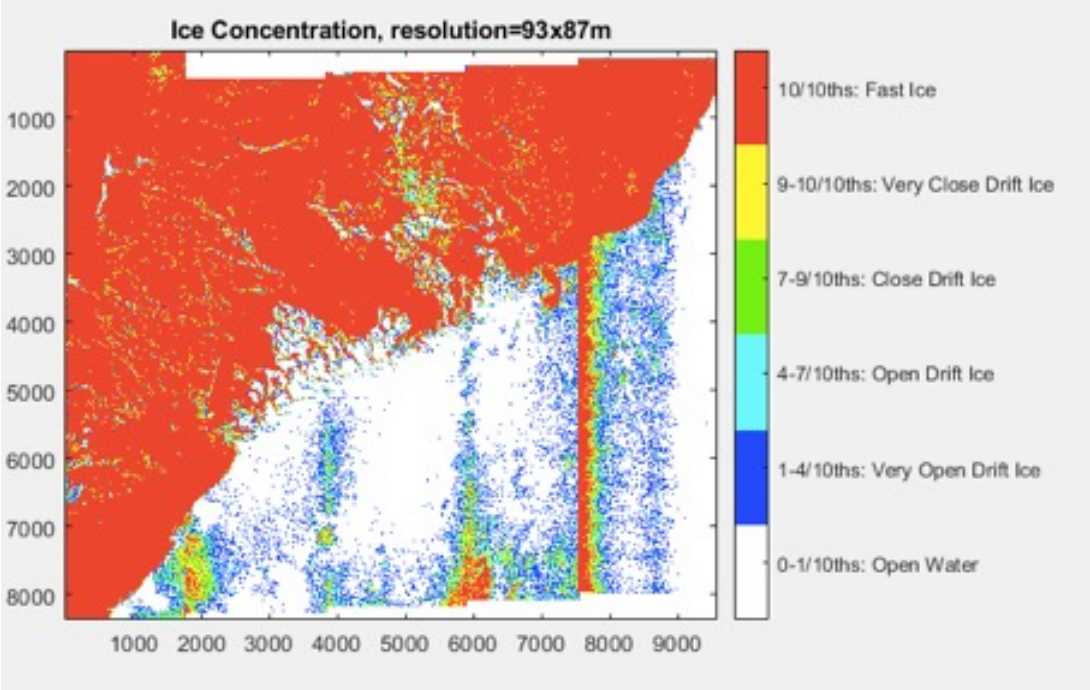

Figure 6.15: Ice concentration map with 93x87 m resolution

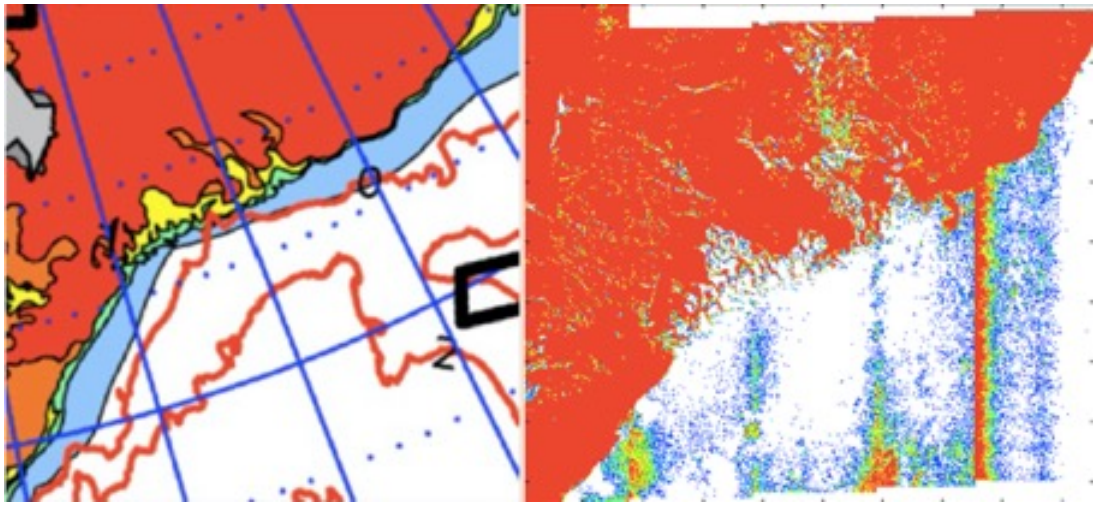

Figure 6.16: 93x87 Ice concentration map vs hand drawn from Met

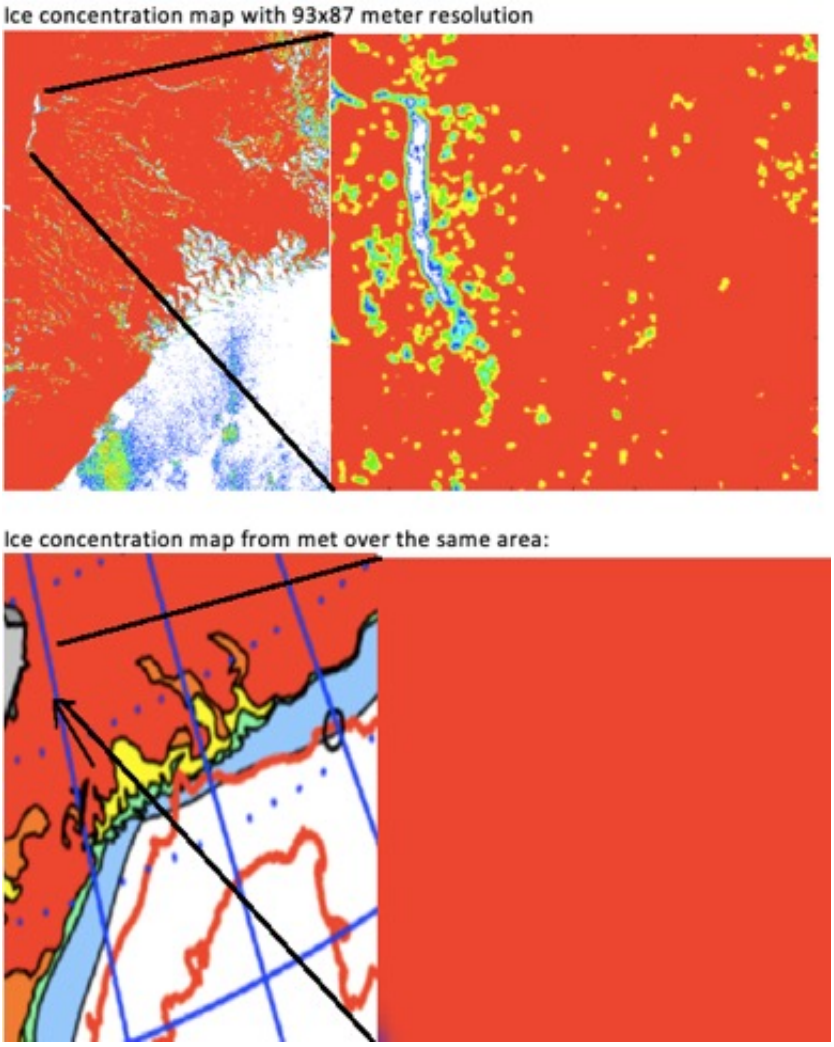

Figure 6.17: Showing small-scale features that only is visible in the high-resolution ice concentration map

Next, the low-resolution sea ice concentration map (930x870 m) is presented.

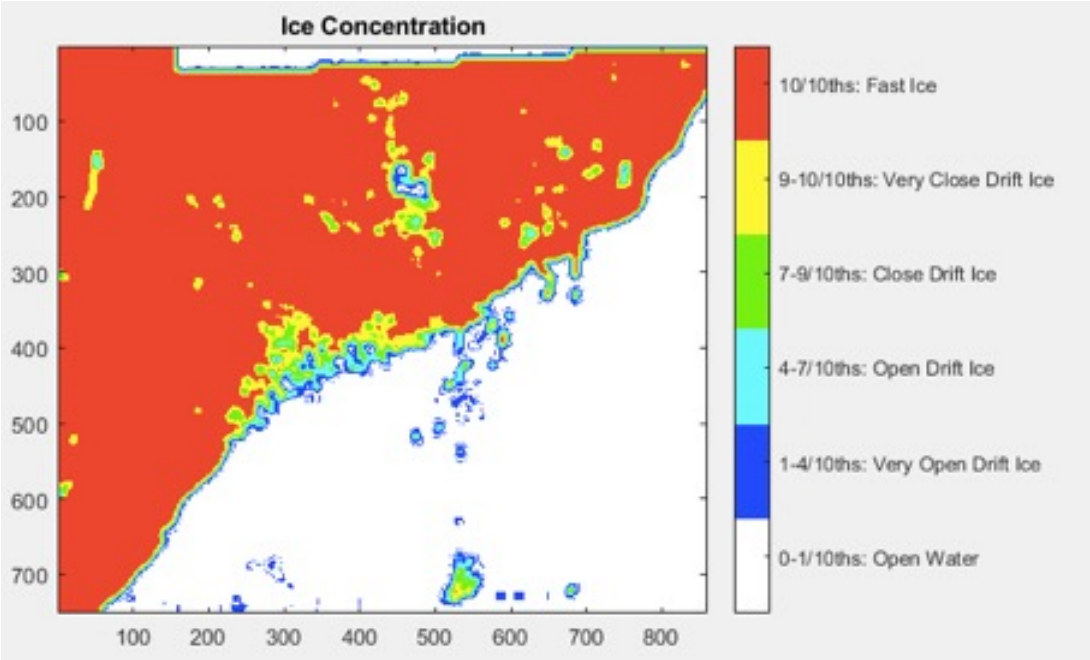

Figure 6.18: Ice concentration map based on ice-water classification with 930x870 m resolution

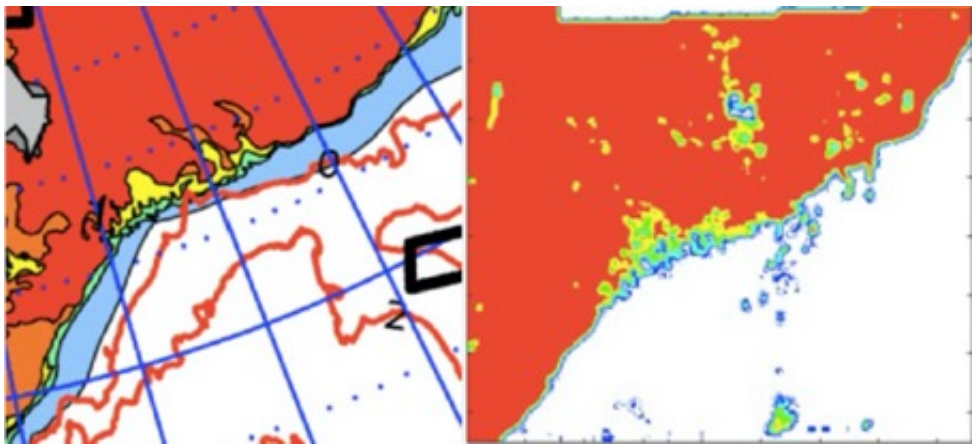

Figure 6.19: Hand drawn vs 930x870 m ice concentration map

6.4.2 Concluding remarks of experiment 4

- The high-resolution sea ice concentration map (93x87 m) shows a lot more details in the ice than the hand drawn maps, such as leads and cracks that can be utilized for ships. However, the maps suffers from thermal noise, which needs to be corrected if these maps are to be used operationally.

- The low-resolution map is less bothered with thermal noise, but shows less details in the ice. It is actually fairly similar to the hand drawn, except some misclassified sea ice in the water, and some misclassified water in the sea ice. However, the hand drawn maps also has some mistakes. For instance, it does not pick up the open water up in the left corner. An important difference between these maps is that the automatic ice concentration map can be processed within a few minutes and delivered in near real time to the ships, while the hand-drawn normally is available several hours after the image is taken.

7

Conclusion

7.1 Summary

This thesis was about ice-water classification on Sentinel-1 EW SLC imagery in the Barents Sea. The aim of the thesis was to evaluate the utility of seven different features for ice-water classification, and thereafter to find the highest achievable, reliable resolution on the ice-water maps. For the first question, it turned out that the highest accuracy was achieved by using the extended polarimetric features geometric brightness, cross-pol ratio and relative kurtosis, with a classification result of 99.29 %. The misclassified pixels were mainly related to thermal noise that occurs at the end of each swath in range direction. Presumably, the accuracy would be close to 100 % if an efficient thermal noise removal method was applied to the image. A simple method to remove this noise was proposed, and gave increased accuracy for the low-resolution classified image. For high-resolution imagery, however, this method must be adjusted in order to work. Moreover, two features that is not found much information about in the literature; HH-HV correlation magnitude and angle, was evaluated. From the results it seems like HH-HV correlation magnitude shows clear separation between ice and water, except for swath 1, and could possibly increase ice-water separability together with the other features, but only if swath 1 is omitted. This feature does not, however, increase the separability between ice types. HH-HV correlation angle, on the other hand, seems useless both for separating ice and water and between ice types.

For the second question, it turned out that the highest achievable resolution on ice-water maps from Sentinel-1 EW images is 46x43, but only if swath 1 is omitted, as this swath is heavily corrupted by thermal noise when few looks are applied. This resolution requires SLC data. There is, however, still some noise-related misclassification in this map over the sea ice. Thus, if reliable maps are required, a 93x87 meter resolution map is possibly the best choice, as this contains considerably less noise. This can be obtained both from SLC and GRD images. Furthermore, the classified image can be used to derive other ice information products, such as ice concentration. This was demonstrated both with low and high resolution. Again, the noise is a problem that needs to be sorted out if reliable high resolution ice concentration maps are to be generated.

7.2 Further work

- There are many improvements that can be done to further increase the ice-water classification accuracy. As mentioned several times, an efficient thermal noise correction on SLC images, that preserves phase information, is the most important factor that could improve the accuracy. Then, tactical sea ice concentration maps with a resolution of 93x87 m could be delivered to ships and off-shore activities in near real time.

- It would also be interesting to test if other features, such as texture features from the grey-level co-occurrence matrix or spatial autocorrelation, could improve the ice-water separation further. Many of them have already been investigated for sea ice classification. For separating solely between ice and water, however, the amount of studies are limited. The optimal combination of features that separates purely between ice and water is yet to be determined.

- This project focused on ice-water classification under winter conditions. The results would, presumably, be different for the summer. The same study should therefore be done during summer also.

- It would be interesting to compare the classification method with other classification methods. For example, how good is this unsupervised classification method compared to a supervised Bayesian classification method. Supervised classification is typically more time-consuming, but gives often better results.

- Only one image was used in this thesis. More reliable results would be obtained if more images were used.

- The ice concentration maps could probably be used to determine the location of the ice edge, for example by saying that the ice edge is where the ice concentration is 50%. One could then create a time series of the ice edge based on several images separated in time, and see how the ice edge has moved in the Barents Sea during the last years or decades.

Bibliography

Armstrong, T. (1972). World meteorological organization. wmo sea-ice nomenclature. terminology, codes and illustrated glossary. edition 1970. geneva, secretariat of the world meteorological organization, 1970.[ix], 147 p.[including 175 photos]+ corrigenda slip.(wmo/omm/bmo, no. 259, tp. 145.). *Journal of Glaciology*, 11(61):148–149.

Bourbigot, M., Johnsen, H., Piantanida, R., and Hajduch, G. (2016). Sentinel-1 product definition. *MDA Document Number: SEN-RS-52-7440*.

Campbell, J. B. and Wynne, R. H. (2011). *Introduction to remote sensing*. Guilford Press.

Chan, Y. K. and Koo, V. C. (2008). An introduction to synthetic aperture radar (sar). *Progress In Electromagnetics Research*, 2:27–60.

Cloude, S. (2010). *Polarisation: applications in remote sensing*. Oxford University Press.

Dierking, W. (2013). Sea ice monitoring by synthetic aperture radar. *Oceanography*, 26(2):100–111.

Doulgeris, A. P. (2013). A simple and extendable segmentation method for multi-polarisation sar images.

Doulgeris, A. P. and Cristea, A. (2018). Incorporating incidence angle variation into sar image segmentation. In *IGARSS 2018-2018 IEEE International Geoscience and Remote Sensing Symposium*, pages 8543–8546. IEEE.

El-Darymli, K., McGuire, P., Gill, E., Power, D., and Moloney, C. (2014). Understanding the significance of radiometric calibration for synthetic aperture radar imagery. In *2014 IEEE 27th Canadian Conference on Electrical and Computer Engineering (CCECE)*, pages 1–6. IEEE.

Elachi, C. and Van Zyl, J. J. (2006). *Introduction to the physics and techniques*

of remote sensing, volume 28. John Wiley & Sons.

Fors, A. S., Brekke, C., Doulgeris, A. P., Eltoft, T., Renner, A., and Gerland, S. (2016). Late summer sea ice segmentation with multi-polarisation sar features in c-and x-band.

Freeman, A. (1993). The effects of noise on polarimetric sar data. In *Proceedings of IGARSS'93-IEEE International Geoscience and Remote Sensing Symposium*, pages 799–802. IEEE.

Henderson, F. M. and Lewis, A. J. (1998). Principles and applications of imaging radar. manual of remote sensing: Volume 2.

Hong, D.-B. and Yang, C.-S. (2018). Automatic discrimination approach of sea ice in the arctic ocean using sentinel-1 extra wide swath dual-polarized sar data. *International journal of remote sensing*, 39(13):4469–4483.

Hunke, E., Notz, D., Turner, A., and Vancoppenolle, M. (2011). The multiphase physics of sea ice: a review for model developers. *The Cryosphere*, 5(4):989–1009.

Johannessen, O. M., Alexandrov, V., Frolov, I. Y., Sandven, S., Pettersson, L. H., Bobylev, L. P., Kloster, K., Smirnov, V. G., Mironov, Y. U., and Babich, N. G. (2006). *Remote sensing of sea ice in the Northern Sea Route: studies and applications*. Springer Science & Business Media.

Krokan, A. (2018). Arctic ship routing.

Lee, J.-S. and Pottier, E. (2009). *Polarimetric radar imaging: from basics to applications*. CRC press.

Lubin, D. and Massom, R. (2006). *Polar Remote Sensing: Volume I: Atmosphere and Oceans*. Springer Science & Business Media.

Marshall, J. and Plumb, R. A. (1989). *Atmosphere, ocean and climate dynamics: an introductory text*, volume 43. Academic Press.

Masson-Delmotte, V., Zhai, P., Pörtner, H., Roberts, D., Skea, J., Shukla, P., Pirani, A., Moufouma-Okia, W., Péan, C., Pidcock, R., et al. (2018). Ipcc, 2018: Summary for policymakers. *Global Warming of*, 1.

Meier, W. N. and Stroeve, J. (2008). Comparison of sea-ice extent and ice-edge location estimates from passive microwave and enhanced-resolution scatterometer data. *Annals of Glaciology*, 48:65–70.

Moen, M.-A., Doulgeris, A. P., Anfinsen, S. N., Renner, A. H., Hughes, N., Gerland, S., and Eltoft, T. (2013). Comparison of feature based segmentation of full polarimetric sar satellite sea ice images with manually drawn ice charts. *The Cryosphere*, 7(6):1693–1705.

Nghiem, S., Kwok, R., Yueh, S., and Drinkwater, M. (1995). Polarimetric signatures of sea ice: 1. theoretical model. *Journal of Geophysical Research: Oceans*, 100(C7):13665–13679.

Onstott, R. and Shuchman, R. (2004). Sar measurements of sea ice. *Chapter*, 3:81–115.

Onstott, R. G. (1992). Sar and scatterometer signatures of sea ice. *Microwave remote sensing of sea ice*, 68:73–104.

O'Connell, B. (2011). Ice hazard radar. In *Proc. of the International Conference on Port and Ocean Engineering under Arctic Conditions (POAC11), Montreal, Canada*.

Park, J.-W., Korosov, A. A., Babiker, M., Sandven, S., and Won, J.-S. (2017). Efficient thermal noise removal for sentinel-1 topsar cross-polarization channel. *IEEE Transactions on Geoscience and Remote Sensing*, 56(3):1555–1565.

Philpot, W. D. and Philipson, W. R. (2012). Remote sensing fundamentals. In *chapter 10 Passive Microwave*. Cornell University.

Sandven, S., Johannessen, O. M., and Kloster, K. (2006). Sea ice monitoring by remote sensing. *Encyclopedia of Analytical Chemistry: Applications, Theory and Instrumentation*.

Scheuchl, B., Flett, D., Caves, R., and Cumming, I. (2004). Potential of radarsat-2 data for operational sea ice monitoring. *Canadian Journal of Remote Sensing*, 30(3):448–461.

Veci, L. (2015). Tops interferometry tutorial.

Wang, L., Scott, K. A., Xu, L., and Clausi, D. A. (2016). Sea ice concentration estimation during melt from dual-pol sar scenes using deep convolutional neural networks: A case study. *IEEE Transactions on Geoscience and Remote Sensing*, 54(8):4524–4533.

Wikipedia contributors (2019). K-means clustering — Wikipedia, the free encyclopedia. [Online; accessed 31-May-2019].

Zakhvatkina, N., Korosov, A., Muckenhuber, S., Sandven, S., and Babiker, M. (2017). Operational algorithm for ice–water classification on dual-polarized radarsat-2 images. *High resolution sea ice monitoring using space borne Synthetic Aperture Radar*.

Zakhvatkina, N., Smirnov, V., and Bychkova, I. (2019). Satellite sar data-based sea ice classification: An overview. *Geosciences*, 9(4):152.